The Early Cambrian bimodal magmatism in the northeastern Siberian Craton

A.V. Prokopiev [a,*], A.K. Khudoley [b], O.V. Koroleva [a], G.G. Kazakova [c], D.K. Lokhov [b], S.V. Malyshev [b], A.I. Zaitsev [a], S.P. Roev [a], S.A. Sergeev [c], N.G. Berezhnaya [c], D.A. Vasiliev [a]

[a] *Diamond and Precious Metal Geology Institute, Siberian Branch of the Russian Academy of Sciences, pr. Lenina 39, Yakutsk, 677980, Russia*
[b] *Saint Petersburg State University, Institute of Geosciences, Universitetskaya nab. 7/9, St. Petersburg, 199034, Russia*
[c] *A.P. Karpinsky Russian Geological Research Institute, Srednii pr. 74, St. Petersburg, 199106, Russia*

Abstract

We present new data on geochemistry, isotopic geochemistry, and geochronology of the Early Cambrian igneous rocks of the northeastern Siberian Craton (Kharaulakh anticlinorium, contact between the Siberian Platform and the West Verkhoyansk sector of the Verkhoyansk fold-and-thrust belt united into an Early Cambrian bimodal complex. This complex comprises trachyrhyolites forming pebbles in conglomerates near the base of the Cambrian succession, overlying trachybasalts, and mafic sills and dikes cutting Neoproterozoic strata. According to chemical composition, the felsic rocks are high-alkali rhyolites and correspond to A-type granites. The high contents of Ta, Nb, Hf, Tb, and Zr in these rocks suggest the presence of enriched mantle material in their magmatic sources. The mafic volcanics are high-Ti trachybasalts and trachydolerites with similar geochemical characteristics corresponding to alkali basalts or OIB. The high $(Tb/Yb)_{PM}$ ratios in these volcanics evidence that their magmatic source was the garnet peridotite mantle located at depths more than 90 km and characterized by a low degree of melting. However, the rhyolites, trachybasalts, and trachydolerites show high positive $\varepsilon_{Nd}(T)$ values (4.2–4.7, 7.5–8.9, and 7.2–8.2, respectively) indicating a depleted mantle source and no crustal contamination. The high $(Nb/Yb)_{PM}$ ratio points to the mixing of magmas from enriched and depleted mantle sources. Mafic magmas might have been generated from a heterogeneous source or interacted with the depleted mantle before intrusion. Both the felsic and the mafic rocks formed in within-plate environments. U–Pb zircon dating yielded concordant ages of 525.6 ± 3.9 and 537.0 ± 4.2 Ma, corresponding to the Early Cambrian age of the rhyolites. The date of 546.0 ± 7.7 Ma obtained for one sample points (with regard to the error) to the Late Vendian–Early Cambrian age. Thus, at the Vendian–Early Cambrian boundary, the northeastern Siberian Platform was subjected to continental rifting accompanied by bimodal magmatism of antidrome evolution. According to paleotectonic reconstructions, this part of the Siberian Craton might have been connected with the eastern margin of Laurentia in the Late Neoproterozoic (Late Riphean–Late Vendian), and continental rifting that started at the Vendian–Cambrian boundary led to their separation. The obtained isotope-geochronological data suggest that the studied bimodal complex began to form at the Vendian–Cambrian boundary and this process terminated no earlier than the end of the Terreneuvian (Tommotian), i.e., the complex formed during rifting for about 20 Myr.

Introduction

The Neoproterozoic–Early Cambrian stage of magmatic activity of the northeastern Siberian Craton was considered by many researchers (Khudoley et al., 2013; Kiselev et al., 2012a,b; Kolodeznikov and Struchkov, 2001; Kolodeznikov et al., 1974; Leonov and Gogina, 1968; Oleinikov et al., 1983; Prokopiev et al., 2011; Shpunt, 1987; Shpunt and Oleinikov, 1989; Shpunt et al., 1979, 1982).

In the northeastern Siberian Platform, the Early Cambrian magmatism was manifested in the Olenek Uplift and in the Kharaulakh anticlinorium of the Verkhoyansk fold–and-thrust belt at the boundary with the platform (Bowring et al., 1993; Khudoley et al., 2013; Kiselev et al., 2012a,b; Kolodeznikov and Struchkov, 2001; Kolodeznikov et al., 1974; Leonov and Gogina, 1968; Nakhabtsev et al., 1971; Oleinikov et al., 1983; Pelechaty, 1996; Pelechaty et al., 1996; Prokopiev et al., 2001,

* Corresponding author.
E-mail address: prokopiev@diamond.ysn.ru (A.V. Prokopiev)

2011; Shpunt, 1987). In the Olenek Uplift, Lower Cambrian explosive breccias (Mongus and Kessyusa Formations) and trachybasalts were described (Smetannikova et al., 2013), and in the Kharaulakh anticlinorium east of it (Chekurovka anticline, Tuora-Siss Ridge), rhyolites from conglomerate pebbles and the overlying trachybasaltic lavas in the basal member of the Lower Cambrian deposits of the Tyuser Formation were examined (Oleinikov et al., 1983). There are also abundant basic intrusions (predominant sills and subordinate dolerite dikes) cutting Neoproterozoic deposits (Khudoley et al., 2013; Prokopiev et al., 2001, 2011).

The Early Cambrian magmatism is associated with continental rifting (Bulgakova, 1991, 1996; Khudoley, 2003; Khudoley and Guriev, 2003; Khudoley et al., 2013) and plume activity (Kiselev et al., 2012a,b). Pelechaty et al. (1996) were the first to recognize these deposits as a Vendian–Early Cambrian bimodal rhyolite–basic complex formed at the synrift stage (~543–530 Ma).

The goal of this work was to present new complex geological materials, including geochemical and isotope data on the Early Cambrian bimodal magmatism in the northeastern Siberian Craton, and to refine the time and geodynamic setting of its manifestation. Study of this stage is important for better understanding of the Early Paleozoic tectonics and geodynamics of Central Asia as a whole (Dobretsov, 2011; Kuzmin et al., 2010) and the Siberian Craton in particular. Research into the geodynamic processes running on the periphery of the Siberian Craton at that time, recognition of the crucial stages in the Late Precambrian and Paleozoic history of North Asia, and reconstruction of the probable plume stages of magmatism are the subject of publications by Dobretsov (2003, 2010), Dobretsov and Vernikovsky (2001), and Dobretsov et al. (2003).

Geologic setting

The study area lies in the core and on the eastern flank of the Chekurovka anticline, in the lower reaches of the Lena River, at the boundary between the northeastern Siberian Platform and the northern flank of the Verkhoyansk fold-and-thrust belt (Fig. 1). Investigations and sampling were performed in the bank exposures along the Lena River, from the mouth of the Ukta Brook in the south to the mouth of the Biskeibit Brook in the north (Fig. 2). Here, an upper Neoproterozoic (Khabarov and Izokh, 2014; Khudoley et al., 2015), Cambrian, and Permian section is exposed (Fig. 3a).

The Neoproterozoic deposits in the bottom are alternating siltstones and sandstones. They are overlain by stromatolite dolomites and limestones giving way to limestones and siltstones. The Vendian (Ediacaran) deposits (Kharayutekh Formation) rest (with erosion and considerable break in sedimentation) upon a rock unit composed of gravelstones and sandstones in the bottom and predominant limestones in the above beds (Khabarov and Izokh, 2014; Semikhatov and Serebryakov, 1983; Shpunt et al., 1979). The Neoproterozoic section was assumed to be rich in volcanic material (Shpunt, 1987; Shpunt et al., 1982).

There is a series of trachydolerite sills and dikes 10–20 to 120 m thick in the Neoproterozoic deposits (Kolodeznikov and Struchkov, 2001; Oleinikov et al., 1983; Prokopiev et al., 2001) (Fig. 4a, b). The total thickness of basic sills in the study area is more than 250 m, and the available unreliable K–Ar dates for two of them are 449 ± 13 and 508 ± 13 Ma (Oleinikov et al., 1983). Rare dikes are feeding channels for the sills, as seen in the exposure opposite to the mouth of the Ukta Brook.

The Lower Cambrian sandstones (Tyuser Formation) overlie (with erosion and considerable break in sedimentation) (Shpunt et al., 1979) the karst surface of the Vendian dolomites and limestones (Bowring et al., 1993; Pelechaty, 1996; Pelechaty et al., 1996). In the section near the mouth of the Biskeibit Brook, the basal deposits of the Tyuser Formation (15 m thick) are cross-bedded medium- and coarse-grained dark gray and brownish-gray sandstones with rare siltstone intercalates (Fig. 3b). They are overlain by a 8 m thick bed of conglomerates composed predominantly (>99%) of pebbles of ultrapotassic trachyryolite porphyry (Prokopiev et al., 2011), up to 20–25 cm in size (Fig. 4c–e). The matrix is formed by coarse-grained sandstone. The presence of acid rocks in the section was first reported by Shpunt (Oleinikov et al., 1983; Shpunt, 1987; Shpunt and Oleinikov, 1989; Shpunt et al., 1979, 1982). In the northeastern platform, however, these rocks are not exposed and occur only in the above-mentioned conglomerate pebbles. The large size of the pebbles suggests a proximal sourceland. The pebbles are usually rounded (Fig. 4d, e). The intimate contacts between some of them (Fig. 4e) do not rule out their burial in the plastic state immediately after the intrusion of trachyrhyolites. U–Pb zircon dating of two pebbles ~20 cm in size yielded an age of 534.6 ± 0.4 Ma (Bowring et al., 1993).

Upsection, the conglomerates are overlain by a 45 m thick basalt flow (Fig. 3b), with distinct pillow trachybasalts (Fig. 4f). These basalts are dated at the Early Cambrian (Khudoley et al., 2013; Kiselev et al., 2012a,b; Oleinikov et al., 1983; Prokopiev et al., 2001, 2011) as it is overlain by essentially carbonate rocks containing skeleton fauna of Early Cambrian age (Missarzhevskii, 1989; Repina et al., 1974). Shpunt (1987) recognized two lava flows, 4 and 48 m thick, in the studied exposure and five thin lava flows in the valley of the Biskeibit Brook 1 km west of it. No mafic igneous bodies were found in the overlying Cambrian deposits. At 15 km to the south of the studied exposure, in the Lena River bank outcrops near the mouth of the Ukta Brook, a basalt flow up to 10 m thick was revealed near the base of Lower Cambrian succession, but the above-described conglomerates were not found there. West of this site, in the Lower Cambrian Mongus (Kessyusa) Formation in the Olenek Uplift, basal sandstones resting with erosion upon Vendian strata are overlain by tuff breccias, tuff conglomerate-breccias, tuff conglomerates (Smetannikova et al., 2013), and pyroclastic breccias. U–Pb dating of zircons from the breccias yielded an age of 543.9 ± 0.24 Ma (Bowring et al., 1993). Upsection, there are basalt flows, tuffs, and trachytes up to 0.5–10 m in thickness (Smetannikova et al., 2013).
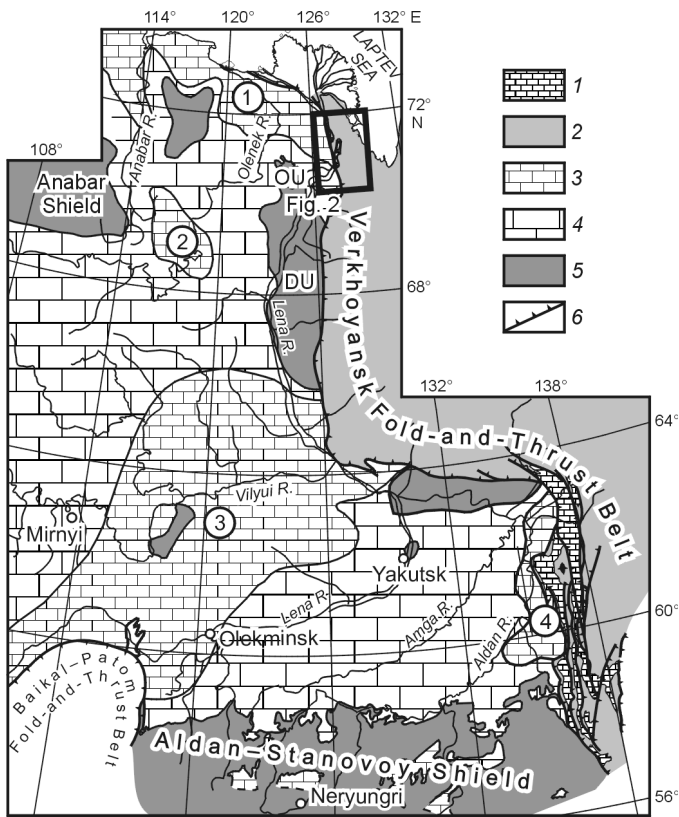
Fig. 1. Vendian–Lower Paleozoic structural stage, after Prokopiev et al. (2001), with modifications and supplement. Verkhoyansk fold-and-thrust belt: *1*, Vendian–Lower Paleozoic deposits; *2*, overlying Phanerozoic deposits; Siberian Platform: *3*, Vendian–Lower Paleozoic deposits 1.5–5.0 km in thickness in sedimentary basins (1, Lower Olenek; 2, Sukhana; 3, Central Yakutian; 4, Aldan–Maya); *4*, elevated areas with Vendian–Lower Paleozoic deposits mostly <1.5 km in thickness; *5*, areas lacking Vendian–Lower Paleozoic deposits (these deposits did not accumulate or were eroded later) (OU, Olenek Uplift; DU, Dzhardzhan Uplift); *6*, front of Phanerozoic orogenic belts.
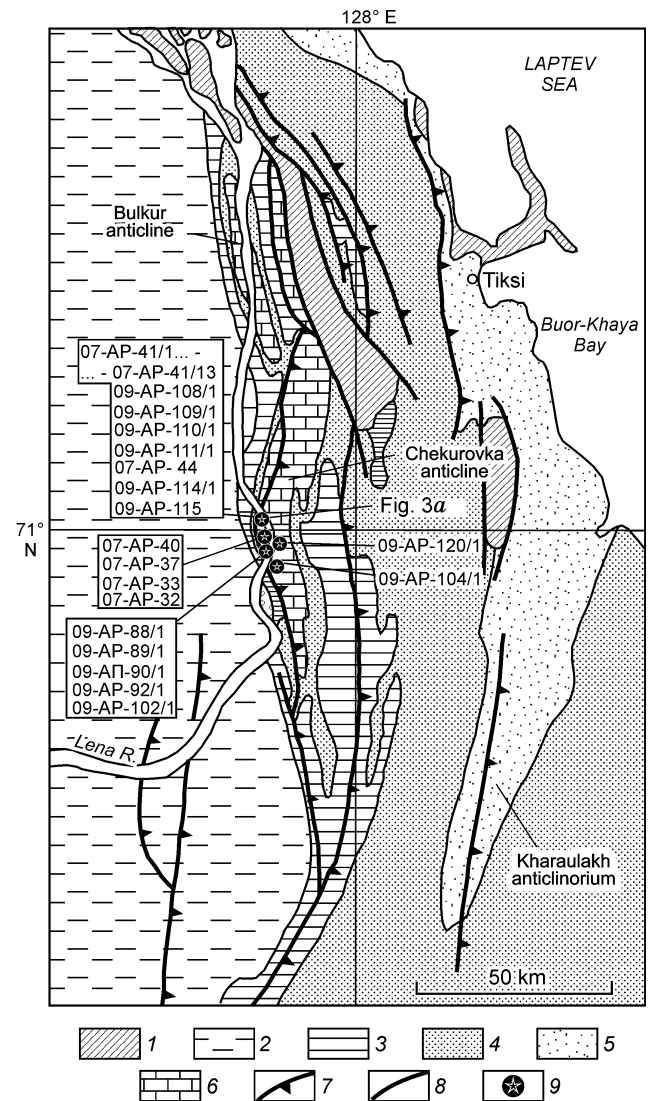

Fig. 2. Schematic geological map of the northern part of the front of the Verkhoyansk fold-and-thrust belt (the north of the Kharaulakh anticlinorium) (Prokopiev and Deikunenko, 2001), with modifications and supplement. The location of the mapped area is shown in Fig. 1. Deposits: *1*, Cenozoic; *2*, Cretaceous; *3*, Triassic and Jurassic; *4*, Permian; *5*, Carboniferous; *6*, Upper Precambrian and Cambrian; *7*, thrusts; *8*, other faults; *9*, location of the studied sections and sampling localities.

The overlying Lower–Upper Cambrian carbonate and terrigenous-carbonate rocks (Sekten, Mayaktakh, and Ogon'or Formations) are overlain by Lower Permian terrigenous strata (Fig. 3*a*).

Petrography of rocks

Trachyrhyolites (quartz-feldspathic rocks) composing pebbles of the Lower Cambrian conglomerates are fine-grained, of porphyritic (or, sometimes, glomeroporphyritic) structure. Phenocrysts amount to ~30–45% and are composed of orthoclase, quartz, and completely altered dark-colored minerals. Orthoclase forms prismatic tablets measuring fractions of mm to 5–7 mm, and quartz occurs as rounded near-prismatic grains of similar size (Fig. 5*a*). Feldspar is partly pelitized (Fig. 5*b*). Dark-colored minerals were initially amphiboles, as evidenced by their morphology. These are pseudomorphs of ore minerals with aggregates of chlorite, secondary amphiboles, and epidote-zoisite minerals and quartz-K-feldspar aggregates (Fig. 5*c*). The matrix is composed of K-feldspar, quartz,

oxide-ore minerals, and chlorite (Fig. 5*d*) and is xenomorphic-granular. The mineral grains are ~0.01–0.03 mm in size. Accessory minerals are zircon, apatite, sulfides, and iron oxides. According to structures, textures, and mineral composition, the rocks can be assigned to subvolcanic potassic trachyrhyolitic porphyry.

The overlying basalt flow is formed by fine-grained trachybasalts of amygdaloidal structure. The rock-forming minerals are plagioclase (45–55%), clinopyroxene (20–40%), titanomagnetite, apatite, and ore minerals (≤5%). The content of crystalline glass varies from 5 to 25% (Fig. 5*e, f*). The rocks are altered by propylitization, which gave rise to chlorite, albite, and, to a smaller extent, carbonates, sericite, and hematite (15 to 25%). In the sample 09-AP-104/1 the
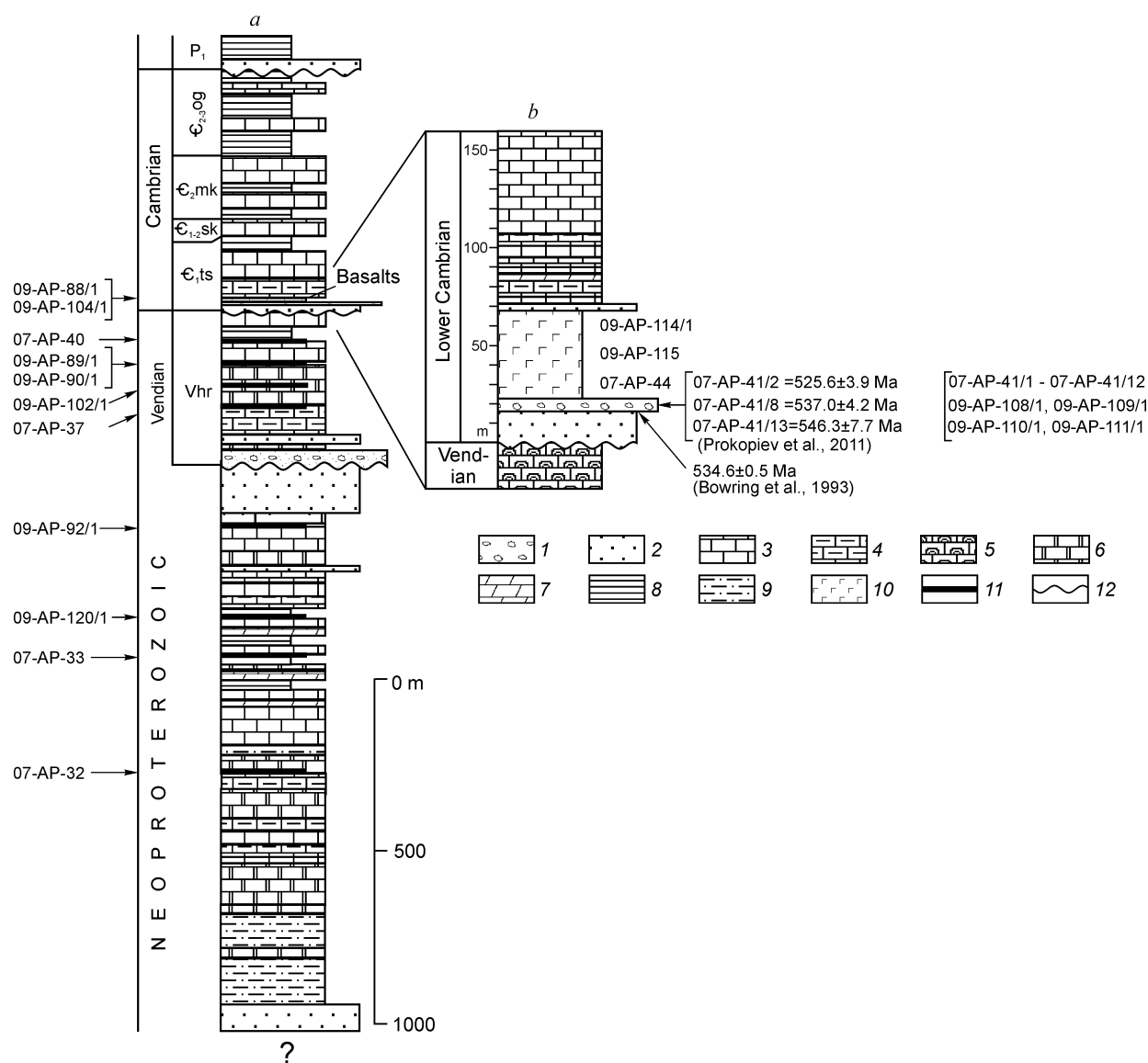
Fig. 3. Stratigraphic column of deposits exposed in the cores of the Chekurovka and Bulkur anticlines (after Prokopiev et al. (2001) and Semikhatov and Serebryakov (1983), with modifications and supplement) (*a*); stratigraphic section in the mouth of the Biskeibit Brook (*b*) (after Prokopiev et al. (2011), with modifications and supplement) and sampling locality. *1*, conglomerates; *2*, sandstones; *3*, limestones; *4*, argillaceous limestones; *5*, organogenic limestones; *6*, dolomites; *7*, marls; *8*, mudstones; *9*, siltstones; *10*, trachybasalts; *11*, trachydolerite sills; *12*, unconformity. Formations: Vhr, Kharayutekh (Vendian); $\mathcal{C}_1$ts, Tyuser; $\mathcal{C}_{1-2}$sk, Sekten; $\mathcal{C}_2$mk, Mayaktakh; and $\mathcal{C}_3$og, Ogon'or (Cambrian).

content of these minerals reaches 50%. The amygdales consist of chlorite, calcite, and epidote (Khudoley et al., 2013).

Sills and dikes in the Neoproterozoic section are composed of same-type trachydolerites. Amygdaloidal structures are revealed at the rock contacts. The amygdales consist mostly of quartz with subordinate calcite, chlorite, analcite, zeolites, and clay mineral. The rock-forming minerals of the trachydolerites are plagioclase of labradorite-andesine composition and Ti-augite; there are also bowlingite pseudomorphs after olivine as well as titanomagnetite. Late- and postmagmatic alterations are expressed as sericitization, carbonatization, and albitization of plagioclases and formation of analcite, orthoclase, and chlorite (Oleinikov et al., 1983).

Analytical technique

The contents of whole-rock major elements were determined in bulk samples by the wet-chemistry method at the Diamond and Precious Metal Geology Institute, Yakutsk. The contents of trace elements were measured by ICP-MS on an Optima 4300DV emission spectrometer and an ELAN 6100 DRC mass spectrometer in the Central Laboratory of the Russian Geological Research Institute, St. Petersburg.

The contents and isotopic compositions of Sm and Nd were determined using a TRITON TI multicollector mass spectrometer in the static mode at the Institute of Precambrian Geology and Geochronology, St. Petersburg. Chemical separation of Sm and Nd was made after the decomposition of the
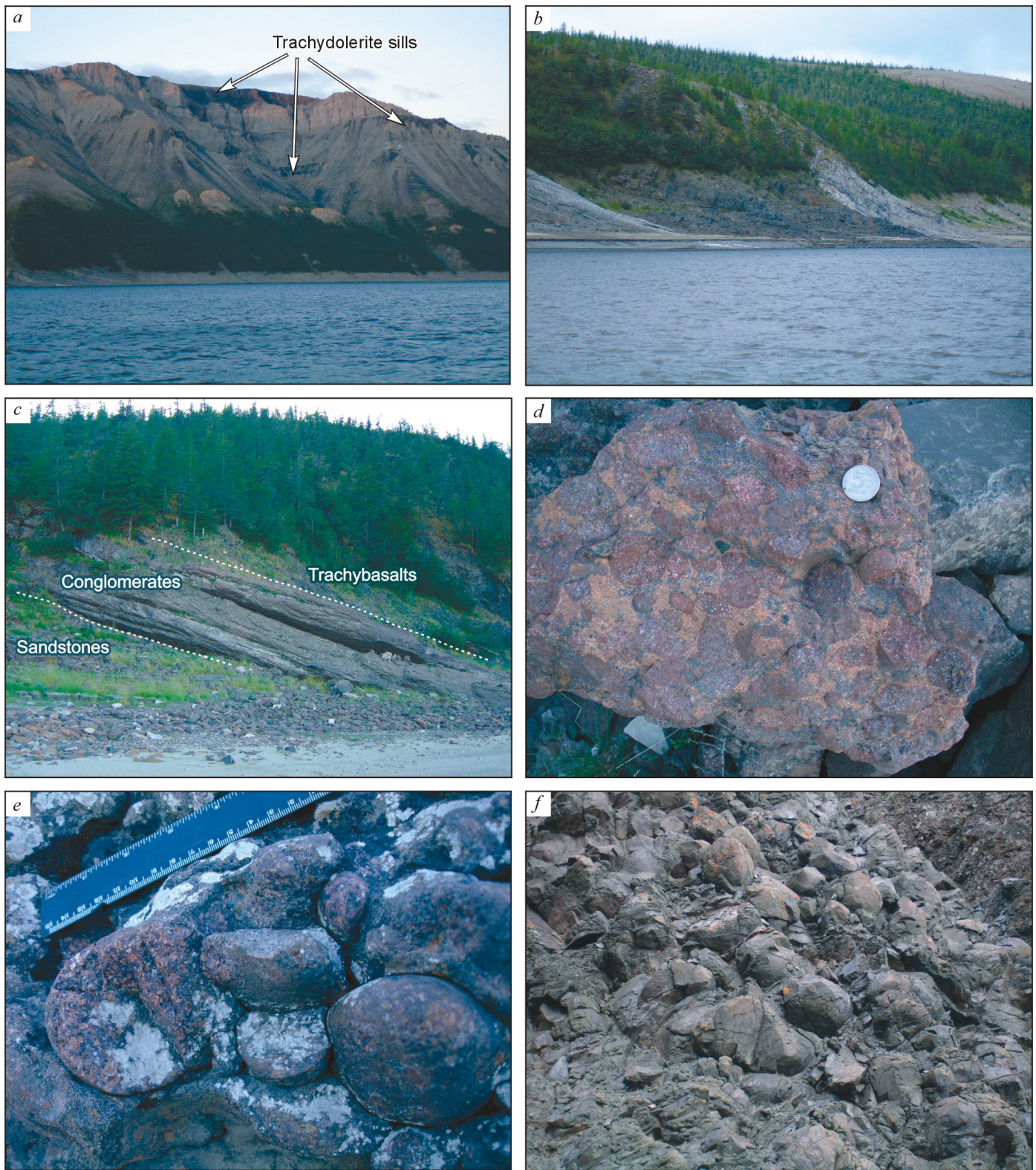
Fig. 4. Trachydolerite sills in the Riphean section of the core of the Chekurovka anticline (*a*, *b*); Lower Cambrian conglomerates near the mouth of the Biskeibit Brook (*c–e*); Early Cambrian pillow trachybasalts (*f*).

bulk samples and minerals in a HF + HNO$_3$ mixture at 110 ℃ and addition of a mixed ^{149}Sm–^{150}Nd indicator. Rare-earth elements were separated by standard cation exchange chromatography, using columns filled with Bio-Rad AG1-X8 resin.

Subsequent separation of Sm and Nd from REE was performed by extraction chromatography in EICHROM columns filled with LN-Spec resin, following the technique proposed by Kotov et al. (1995). The blank test for the laboratory

Fig. 5. Photomicrographs of igneous rocks exposed in the core of the Chekurovka anticline. Trachyrhyolites from conglomerate pebbles: *a*, porphyritic K-feldspar and quartz grains, sample 07-AP-41/2, ×40, nicols ×, *b*, pelitized K-feldspar grain, sample 07-AP-41/8, ×40, nicols ∥; *c*, pseudomorph after amphibole (oxide-ore minerals with assemblage of chlorite, secondary amphiboles, and epidote–zoisite minerals), rimme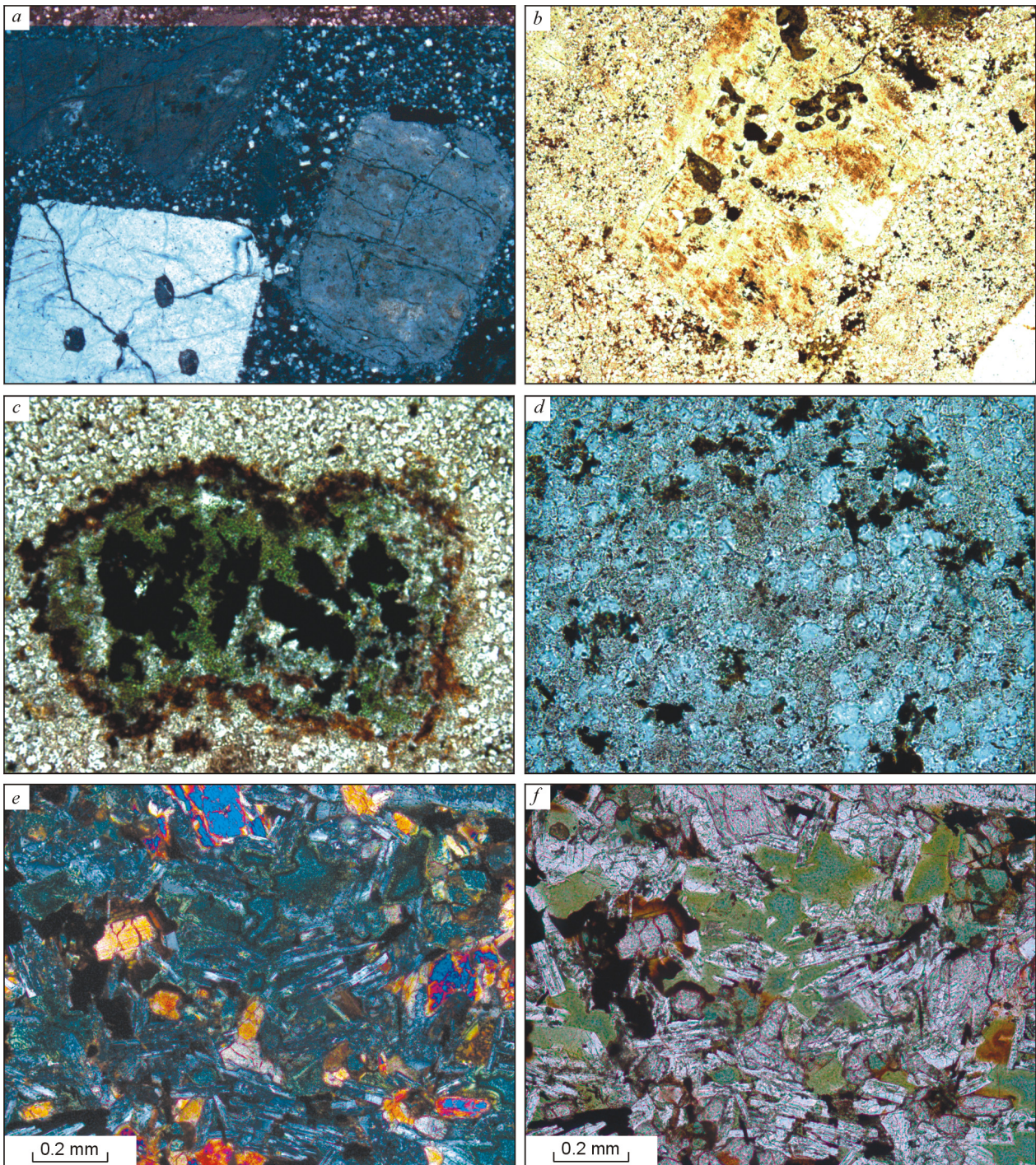d by semitransparent iron oxides, sample 07-AP-41/13, ×40, nicols ∥; *d*, matrix composed of K-feldspar, quartz, ore minerals, and chlorite, sample 07-AP-41/13, ×200, nicols ∥; *e, f*, hydrothermally altered basalts, sample 09-AP-115 (Khudoley et al., 2013). Magmatic clinopyroxene and plagioclase are replaced by chlorite (propylitization).

contamination showed 0.03–0.1 ng Sm and 0.1–0.2 ng Nd. The measured $^{143}Nd/^{144}Nd$ ratios were normalized to $^{146}Nd/^{144}Nd = 0.7219$ and reduced to $^{143}Nd/^{144}Nd = 0.512117$ of the JNdi-1 International Nd-standard. The weighted average value of $^{143}Nd/^{144}Nd$ in this standard during the analysis was 0.512105 ± 4 (2σ, $n = 25$). The accuracy of measurement of

$^{147}Sm/^{144}Nd$ and $^{143}Nd/^{144}Nd$, estimated from a series of analyses of the BCR-2 standard, is ±0.3% and ±0.002%, respectively. The $\varepsilon_{Nd}(t)$ values and model ages $T_{Nd}(DM)$ were calculated using the modern isotope ratios of CHUR ($^{143}Nd/^{144}Nd = 0.512638$ and $^{147}Sm/^{144}Nd = 0.1967$ (Jacobsen and Wasserburg, 1984)) and DM ($^{143}Nd/^{144}Nd = 0.513151$

and $^{147}Sm/^{144}Nd = 0.2136$ (Golstein and Jacobsen, 1988)). To take into account possible fractionation of Sm and Nd during the intracrustal processes, we calculated the two-stage model ages T_{Nd}(DM-2st) (Liew and Hofmann, 1988).

Rb-Sr isotope analyses were carried out on a MI-1201-T mass spectrometer with tantalum tapes in the single-beam mode at the Diamond and Precious Metal Geology Institute, Yakutsk. The contents of Rb were determined by the isotope dilution method, and the contents of Sr, by the double isotope dilution method. The Sr isotope composition was estimated without using an indicator. For analysis, the sample was decomposed in Teflon bombs with a HF+HClO$_4$ (3:1) mixture in the autoclave mode at 200 °C for 8 h. The elements were separated by ion exchange chromatography, using columns with Dowex 50×8 resin (200–400 mesh). The inner error of measurement of isotope ratios was within 0.05%. The reproducibility of parallel runs during the measurement of ^{87}Rb and ^{88}Sr contents and $^{87}Sr/^{86}Sr$ was no more than 0.5, 0.4, and 0.03%, respectively. The total contents of Rb and Sr in the blank tests were 0.006–0.010 and 0.03–0.05 ppm, respectively. The accuracy and reproducibility of isotope measurements were controlled by analysis of the Karbonat-70 isotope standard, whose average ($n = 8$) normalized value of $^{87}Sr/^{86}Sr$ was 0.7089 ± 0.0002.

For U–Pb isotope studies we used the same samples as for the Rb–Sr and Sm–Nd ones. Zircon monofraction was separated following a standard scheme: grinding, sieving into size fractions, passing of the fraction of <0.25 mm through a centrifugal concentrator, electromagnetic treatment of the obtained heavy fraction, and the final treatment of the concentrate with a heavy liquid. Then, several tens of grains were selected under a binocular, and the most typical ones were used for isotope studies. U–Pb zircon dating was performed on a SHRIMP-II ion microprobe at the Center of Isotope Studies of the Russian Geological Research Institute, St. Petersburg. The selected zircon grains were implanted into

epoxy resin together with grains of the TEMORA and 91500 standard zircons and then smoothed and polished to approximately half the thickness. The surface dots for dating were chosen based on optical (in transmitted and reflected light) and cathodoluminescence (CL) images depicting the internal structure and zoning of zircons.

The U/Pb isotope ratios were measured on SHRIMP-II following the technique of Williams (1998). The current of a primary beam of molecular negative oxygen ions was ~2.5–4 nA, and the crater diameter was $~15 \times 10$ µm.

The obtained data were processed using the SQUID program (Ludwig, 2001). The U/Pb isotope ratios were normalized to the value of 0.0668 of the TEMORA standard zircon, corresponding to an age of 416.75 Ma (Black et al., 2003). The errors of analyses (isotope ratios and ages) are at the 1σ level, and the errors of calculation of concordant ages are at the 2σ level. Concordia diagrams were constructed using the ISOPLOT program (Ludwig, 2003).

Geochemistry of rocks

The contents of major and trace elements in the rocks of the Early Cambrian bimodal complex of the Chekurovka anticline are listed in Tables 1 and 2.

Rhyolites from Lower Cambrian conglomerates. The studied felsic rocks are high-alkali rhyolites of high-K series according to their petrochemical characteristics (Table 1). On the classification diagrams, their composition points are localized mostly in the fields of rhyolites (Fig. 6a) and trachytes (close to the fields of comendites and pantellerites, Fig. 6b): SiO$_2$ = 70.04–74.85%, Al$_2$O$_3$ = 12.05–12.80%, Na$_2$O + K$_2$O = 9.01–10.55%, with a predominance of K$_2$O (8.51–9.91%) and minor Na$_2$O (0.09–1.4%). Most of the rocks are slightly peraluminous granites, whereas metaluminous varieties are scarce (ASI = 0.95–1.16, A/NK ≥ 1) (Fig. 7a).

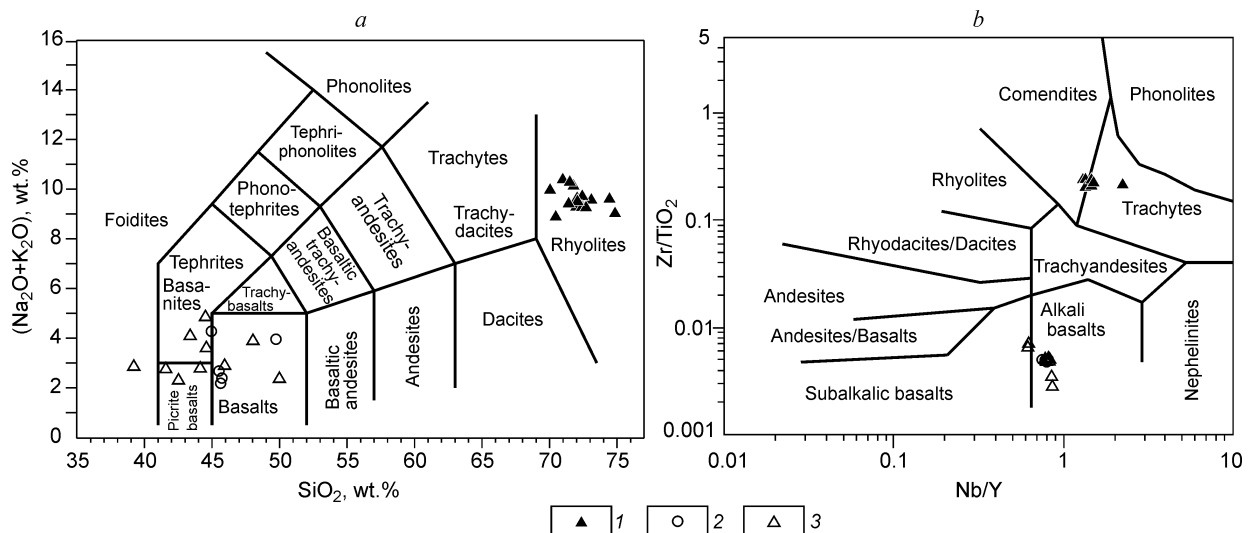Fig. 6. Classification diagrams for rocks of the bimodal complex from the Chekurovka anticline. a, (Na$_2$O+K$_2$O)–SiO$_2$ diagram (Le Bas et al., 1986); b, Zr/TiO$_2$–Nb/Y (Winchester and Floyd, 1977). 1, rhyolites; 2, trachybasalts; 3, trachydolerites.

Table 1. Contents of major (wt.%) and trace (ppm) elements in rhyolites of the Early Cambrian bimodal complex of the Chekurovka anticline

Component	07-AP-41/2	07-AP-41/8	07-AP-41/13	09-AP-108/1	09-AP-109/1	09-AP-110/1	09-AP-111/1	07-AP-41/1	07-AP-41/3	07-AP-41/4	07-AP-41/5	07-AP-41/6	07-AP-41/7	07-AP-41/9	07-AP-41/10	07-AP-41/11	07-AP-41/12
SiO_2	74.85	72.13	72.05	73.1	70.98	70.04	71.78	72.34	72.43	70.46	71.98	72.41	71.5	74.44	72.7	72.07	71.42
TiO_2	0.28	0.36	0.35	0.33	0.33	0.3	0.3	0.35	0.34	0.34	0.33	0.36	0.34	0.28	0.36	0.35	0.34
Al_2O_3	12.05	12.18	12.2	12.1	12.41	12.41	12.8	12.27	12.64	12.09	12.18	12.63	12.64	11.98	12.41	11.98	12.2
Fe_2O_3	1.04	2.18	2.75	1.47	2.3	2.41	1.73	0.93	1.85	3.5	2.52	2.08	1.82	1.24	1.66	3.57	1.38
FeO	1.12	1.2	0.94	1.15	1.82	1.35	0.97	1.54	1.13	1.71	0.96	1.21	1.14	0.99	1.29	0.84	1.48
MnO	0.00	0.00	0.00	0.00	0.00	0.00	0.00	0	0	0	0	0	0	0	0	0	0.02
MgO	0.11	0.39	0.26	0.61	0.44	1.77	0.93	0.49	0.3	0.34	0.32	0.45	0.28	0.26	0.32	0.3	0.42
CaO	0.18	0.51	0.33	0.84	0.79	0.96	0.5	0.93	0.36	0.9	0.6	0.27	0.63	0.21	0.33	0.21	1.14
Na_2O	0.5	0.42	0.33	0.58	0.66	0.27	1.4	0.27	0.47	0.29	0.9	0.34	0.36	0.39	0.09	0.47	0.34
K_2O	8.51	9.02	9.29	8.97	9.71	9.68	8.71	9.13	9.23	8.58	8.37	8.92	9.91	9.2	9.15	9.02	9.06
H_2O^-	0.12	0.12	0.18	0.00	0.08	0.06	0.00	0.12	0.24	0.12	0.08	0.12	0.2	0.14	0.14	0.18	0.2
H_2O^+	0.15	0.55	0.27	0.85	0.70	0.97	0.85	0.62	0.3	0.46	0.29	0.49	0.15	0.27	0.47	0.43	0.66
LOI	0.00	0.07	0.18	0.00	0.00	0.00	0.05	0.32	0.32	0.32	0.39	0.12	0.24	0.3	0.14	0.15	0
P_2O_5	0.05	0.06	0.05	0.05	0.05	0.05	0.05	0.04	0.05	0.06	0.05	0.05	0.03	0.04	0.06	0.05	0.05
CO_2	0.78	0.26	0.27	0.00	0.00	0.22	0.00	0.55	0.27	0.55	0.27	0.27	0.53	0	0.27	0	0.81
S	0.08	0.00	0.06	0.05	0.03	0.04	0.04	0	0.01	0.05	0.18	0.25	0.2	0.04	0.22	0.03	0.1
Total	99.71	99.34	99.34	100.10	100.22	100.47	100.11	99.9	99.94	99.77	99.42	99.97	99.97	99.78	99.61	99.65	99.62
Sc	1.68	1.92	1.83	1.99	2.79	2.6	2.69	–	–	–	–	–	–	–	–	–	–
V	18.5	29.1	28.4	27.2	24.4	25.6	12.7	–	–	–	–	–	–	–	–	–	–
Cr	282	250	173	231	235	195	197	–	–	–	–	–	–	–	–	–	–
Co	2.68	3.29	2.86	3.57	3.38	3.58	5.91	–	–	–	–	–	–	–	–	–	–
Ni	16.8	17.5	16	19.7	20.2	13.5	17.7	–	–	–	–	–	–	–	–	–	–
Rb	120	104	111	113	98.9	112	95.8	–	–	–	–	–	–	–	–	–	–
Sr	19.7	35	29.4	26.3	33.1	44.4	28.5	–	–	–	–	–	–	–	–	–	–
Y	57.3	61.7	58.7	36.4	56	60.3	68.5	–	–	–	–	–	–	–	–	–	–
Zr	687	745	742	715	743	714	723	–	–	–	–	–	–	–	–	–	–
Nb	82.1	86.4	92.1	80.9	85.3	89.6	88.6	–	–	–	–	–	–	–	–	–	–
Ba	180	323	273	262	274	411	319	–	–	–	–	–	–	–	–	–	–
La	54.9	91.6	78.6	85.3	102	86.7	42.4	–	–	–	–	–	–	–	–	–	–
Ce	126	202	166	202	223	190	106	–	–	–	–	–	–	–	–	–	–
Pr	16.8	26.5	21.9	25.4	29.6	24.2	12.9	–	–	–	–	–	–	–	–	–	–
Nd	65.2	106	82	106	122	98.5	53.3	–	–	–	–	–	–	–	–	–	–
Sm	12.3	20.5	15.1	19.7	22.7	19.5	11.9	–	–	–	–	–	–	–	–	–	–
Eu	1.69	2.59	2.13	2.33	3	2.43	1.87	–	–	–	–	–	–	–	–	–	–
Gd	9.92	14.4	12.2	12.9	16.4	14.3	10.9	–	–	–	–	–	–	–	–	–	–
Tb	1.58	2.05	1.84	1.6	2.13	2.16	1.99	–	–	–	–	–	–	–	–	–	–
Dy	9.42	11.1	10.9	7.65	10.8	12	12.7	–	–	–	–	–	–	–	–	–	–
Ho	2.11	2.33	2.25	1.48	2.07	2.42	2.64	–	–	–	–	–	–	–	–	–	–
Er	6.37	6.52	6.35	4.62	6.63	7.33	7.57	–	–	–	–	–	–	–	–	–	–
Tm	0.87	0.95	1.03	0.74	1.05	1.04	1.08	–	–	–	–	–	–	–	–	–	–
Yb	5.52	6.29	6.32	4.16	5.94	6.63	7.03	–	–	–	–	–	–	–	–	–	–
Lu	0.8	0.88	0.92	0.62	0.97	0.98	0.97	–	–	–	–	–	–	–	–	–	–
Hf	16.2	16.6	16.5	16.9	16.2	16.3	16.8	–	–	–	–	–	–	–	–	–	–
Ta	5.5	5.05	5.08	5.88	5.3	5.35	5.42	–	–	–	–	–	–	–	–	–	–
Pb	3.71	4.24	5.46	3.89	6.05	4.52	3.14	–	–	–	–	–	–	–	–	–	–
Th	12.4	10.6	10.4	12.1	10.5	10.2	10.4	–	–	–	–	–	–	–	–	–	–
U	2.3	2.07	2.77	1.51	2.51	3.33	2.76	–	–	–	–	–	–	–	–	–	–
ASI	1.16	1.07	1.09	0.99	0.95	0.98	1.02	–	–	–	–	–	–	–	–	–	–
Eu/Eu*(n)	0.48	0.468	0.48	0.45	0.46	0.44	0.50	–	–	–	–	–	–	–	–	–	–
Nb/Y	1.43	1.40	1.57	2.22	1.52	1.49	1.29	–	–	–	–	–	–	–	–	–	–
$(La/Sm)_n$	2.88	2.88	3.36	2.80	2.90	2.87	2.30	–	–	–	–	–	–	–	–	–	–
$(La/Lu)_n$	7.35	11.16	9.16	14.74	11.27	9.48	4.68	–	–	–	–	–	–	–	–	–	–
$(La/Yb)_n$	9.23	13.52	11.54	19.03	15.94	12.14	5.60	–	–	–	–	–	–	–	–	–	–

Note. Here and in Table 2: Eu/Eu*(n) = $(Eu_n)/(Sm_n \cdot Gd_n)^{0.5}$, the contents of elements are chondrite-normalized after Sun and McDonough (1989). ASI (mol) = $Al_2O_3/(CaO + Na_2O + K_2O)$.

Table 2. Contents of major (wt.%) and trace (ppm) elements in basites of the Early Cambrian bimodal complex of the Chekurovka anticline

| Component	Trachydolerites										Trachybasalts				
	07-AP-32	07-AP-33	07-AP-37	07-AP-40	09-AP-89/1	09-AP-90/1	09-AP-91/1	09-AP-92/1	09-AP-102/1	09-AP-120/1	07-AP-44	09-AP-88/1	09-AP-104/1	09-AP-114/1	09-AP-115
SiO_2	44.13	39.2	42.51	44.58	45.93	48.03	49.99	44.51	41.57	43.38	45.64	45.73	49.74	45.51	44.95
TiO_2	4.6	6.39	3.45	3.81	3.47	2.49	2.42	3.93	6.02	4.15	3.44	3.79	3.67	3.49	3.6
Al_2O_3	14.12	11.69	13.51	13.97	14.52	14.7	13.56	14.82	12.05	14.03	14.19	14.56	14.74	15.05	14.58
Fe_2O_3	5.65	6.9	6.26	4.95	3.51	2.38	3.09	6.25	8.07	5.87	5.22	5	4.02	6.17	9.34
FeO	8.73	10.35	7.31	9.21	10	9.97	9.98	9.12	9.75	8.49	8.17	9.53	6.36	7.64	6.21
MnO	0.23	0.2	0.22	0.2	0.18	0.22	0.21	0.16	0.21	0.19	0.2	0.21	0.3	0.18	0.15
MgO	6.62	5.58	5.41	7.2	6.95	6.45	6.44	3.96	5.81	6.91	6.15	6.5	7.41	7.62	6.51
CaO	8.52	11.6	11.43	8.37	10	8.23	10.42	9.69	10.56	8.23	11.13	9.78	8.29	9.09	8.19
Na_2O	2.1	2.27	1.76	2.61	2.08	2.5	1.75	3.74	2.15	3.34	1.7	1.87	3.18	1.87	1.73
K_2O	0.67	0.57	0.53	0.98	0.8	1.38	0.6	1.1	0.59	0.74	0.48	0.52	0.77	0.8	2.54
H_2O^-	0.26	0.18	0.5	0.22	0.44	0.29	0.38	0.13	0.39	0.19	0.36	1.28	0.25	1	0.52
H_2O^+	2.79	2.6	2.3	2.9	2.02	1.99	0.91	1.44	1.3	3.72	1.86	1.71	1.54	2.05	2.27
LOI	0.42	0	0	0.11	0	0.8	0	0	0	0	0.05	0	0	0	0
P_2O_5	0.46	0.39	0.35	0.38	0.32	0.26	0.24	0.54	0.38	0.47	0.33	0.35	0.38	0.33	0.33
CO_2	0	2.1	4.37	0.27	0.27	0	0	0.77	1.82	0.44	0.81	0	0	0	0
S	0.31	0.36	0.11	0.09	0.02	0.05	0.18	0.41	0.3	0.19	0.08	0.13	0.08	0.02	0.08
Total	99.61	100.38	100.02	99.85	100.51	99.74	100.17	100.57	100.97	100.34	99.81	100.96	100.73	100.82	101.00
Sc	29.9	45	32.7	30.8	38.7	39.3	44.1	30.1	53.5	33.2	31	38.1	38.9	38.7	39.6
V	379	602	355	333	380	301	306	459	658	349	339	393	359	329	347
Cr	97.5	27.3	99.2	90.6	152	219	367	54.9	94.8	127	122	116	144	118	111
Co	47.4	59.1	41.1	47.7	50.9	43.2	47	44.7	57.7	50.2	56.7	54.4	49.7	44.7	41.1
Ni	55.5	51.4	52.1	55.2	63.8	64.8	77	13.8	35.3	63.6	81.1	55.8	56.9	56.1	49.2
Rb	11.1	10.1	8.37	10.6	11.9	21.9	13.3	12.1	8.03	18.6	7.54	8.32	4.07	5.44	20.8
Sr	808	779	357	589	373	604	247	325	384	789	323	353	312	342	463
Y	25.2	22.9	26.9	23.5	26.9	31.8	29.2	30.4	25.4	23.3	27.7	29.4	28.4	27.9	29.4
Zr	180	151	165	161	166	160	147	206	171	148	177	181	184	170	181
Ba	240	432	134	1240	–	–	–	–	–	–	144	156	392	228	296
La	18.9	14.5	16.9	15.8	17	16.9	15.9	21.6	16.1	17	17.3	18.3	17.7	17.5	20
Ce	43.8	34.2	39.6	38	40.4	39.1	35.7	51.2	38.9	40.8	40.1	44.3	42.1	40.5	43.9
Pr	6.16	5.15	5.55	5.56	5.56	4.98	4.82	7.01	5.39	5.72	5.58	5.91	5.53	5.49	5.8
Nd	29	24.1	25.5	25.3	27.2	25.1	23.7	36.2	28.5	28	25.5	29.4	28.3	26.5	28.1
Sm	6.88	5.75	6.19	6.06	6.89	6.15	5.69	9.47	7.31	6.61	6.28	7.15	7.23	6.62	6.47
Eu	3.13	2.55	2.25	2.52	2.11	1.87	1.79	3.52	2.65	2.73	2.09	2.14	1.95	2.09	2.29
Gd	6.83	5.65	5.82	6	6.39	6.21	5.47	7.71	6.76	6.43	5.93	6.73	6.72	6.49	6.52
Tb	0.88	0.77	0.85	0.83	0.98	1.02	0.86	1.1	1	0.96	0.86	1.04	0.99	0.97	1.1
Dy	5.05	4.74	5.2	5.03	5.57	6.01	5.83	5.98	5.2	5.02	5.35	5.79	5.71	5.48	6.02
Ho	1.08	0.93	1.06	0.95	1.08	1.24	1.18	1.18	1.05	0.98	1.11	1.15	1.06	1.12	1.15
Er	2.42	2.28	2.56	2.31	2.88	3.52	3.32	3.22	2.67	2.59	2.79	3.16	3.06	2.98	2.97
Tm	0.29	0.3	0.31	0.31	0.42	0.5	0.49	0.46	0.37	0.33	0.34	0.42	0.45	0.4	0.43
Yb	2	1.81	2.14	1.79	2.25	2.84	2.7	2.37	2.06	1.85	2.16	2.46	2.08	2.37	2.3
Lu	0.29	0.27	0.32	0.27	0.34	0.44	0.42	0.36	0.31	0.31	0.31	0.4	0.33	0.35	0.34
Hf	4.34	3.91	3.92	3.86	4	4.22	3.79	5.08	4.18	3.65	4.27	4.39	4.68	4.52	4.87
Ta	1.52	1.22	1.29	1.26	1.34	1.25	1.17	1.45	1.45	1.33	1.29	1.7	1.46	1.43	1.51
Pb	< 1	2.02	2.14	2.68	1.73	1.69	1.85	1.41	1.22	1.85	2.09	3.01	2.11	2.67	4.08
Th	1.29	1	1.29	1.04	1.14	1.78	1.74	1.55	1.18	1.11	1.38	1.47	1.53	1.43	1.43
U	0.43	0.29	0.41	0.33	0.36	0.64	0.53	0.51	0.52	0.49	0.44	0.43	0.57	0.42	0.38
Cu	–	–	–	–	83	162	162	22.4	49.9	45.5	0	96	465	22.9	36.7
Zn	–	–	–	–	82.2	96.6	112	176	156	140	–	141	147	127	140
Nb	–	–	–	–	22.3	19.8	18.3	23.7	21.8	19.8	20.9	23.5	23.4	22.2	23.2
Eu/Eu*(n)	1.40	1.37	1.15	1.28	0.97	0.93	0.98	1.26	1.15	1.28	1.05	0.94	0.86	0.98	1.08
$(La/Lu)_n$	6.98	5.76	5.66	6.27	5.36	4.12	4.06	6.43	5.57	5.88	5.98	4.90	5.75	5.36	6.30
$(La/Yb)_n$	6.78	5.75	5.66	6.33	5.42	4.27	4.22	6.54	5.61	6.59	5.75	5.34	6.10	5.30	6.24
Tb/Yb	0.44	0.42	0.40	0.46	0.44	0.36	0.32	0.46	0.49	0.52	0.40	0.42	0.48	0.41	0.48
La/Yb	9.45	8.01	7.90	8.83	7.56	5.95	5.89	9.11	7.82	9.19	8.01	7.44	8.51	7.38	8.70
La/Sm	2.75	2.52	2.73	2.61	2.47	2.75	2.79	2.28	2.20	2.57	2.75	2.56	2.45	2.64	3.09
Nb/Y	–	–	–	–	0.83	0.62	0.63	0.78	0.86	0.85	0.75	0.80	0.82	0.80	0.79
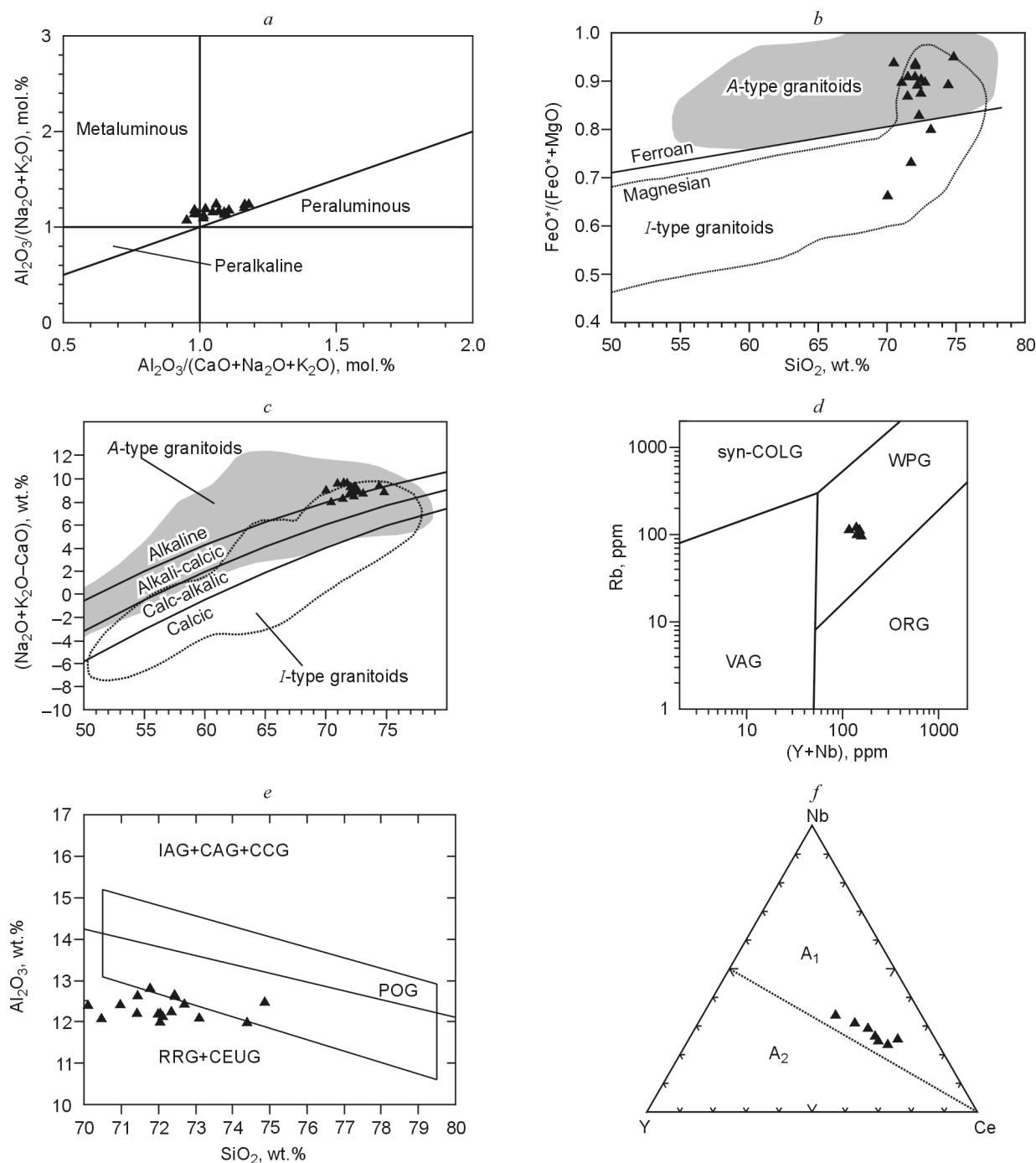
Fig. 7. Diagrams for rhyolites of the bimodal complex from the Lower Cambrian conglomerates. *a*, A/NK–A/CNK (Miniar and Piccoli, 1989); *b*, FeO*/(FeO*+ MgO)–SiO$_2$ (Frost and Frost, 2008; Frost et al., 2001); *c*, (Na$_2$O+K$_2$O–CaO)–SiO$_2$ (Frost and Frost, 2008; Frost et al., 2001); *d*, Rb–(Y+Nb) (Pearce et al., 1984) (fields of granitoids of: VAG, volcanic arcs, ORG, oceanic ridges, WPG, within-plate, syn-COLG, syncollisional); *e*, Al$_2$O$_3$–SiO$_2$ (Maniar and Piccoli, 1989) (fields of granitoids of: IAG, island arcs, CAG, continental arcs, CCG, continental-collision settings, POG, postorogenic, RRG, rift-related, CEUG, continental epiorogenic uplifts); *f*, Nb–Y–Ce (Eby, 1992) (fields of granites with geochemical characteristics of: A$_1$, oceanic-island, within-plate, and rift zone basalts; A$_2$, island-arc and continental-margin basalts).

The low contents of MgO (0.11–1.77%), CaO (0.18–0.96%), and TiO$_2$ (0.28–0.36%) are in correlation with the mineral composition of rocks. The low contents of H$_2$O$^+$ (<1) and CO$_2$ (<0.8) and the low LOI values (<0.32) indicate that the rocks virtually did not undergo secondary alterations. In most of geochemical features the studied trachyrhyolites correspond to *A*-type granites. They are enriched in Fe and are assigned to ferroan *A*-type granites or alkali granites (Frost and Frost, 2008; Frost et al., 2001) (Fig. 7*b*, *c*). On the discrimination diagrams of Pearce et al. (1984), in particular, the Rb–(Y+Nb) ones (Fig. 7*d*), the composition points of the rocks fall in the field of within-plate granites, and on the discrimination diagrams of Maniar and Piccoli (1989) they lie in the fields of rift-related granitoids (Fig. 7*e*). The granites are rich in
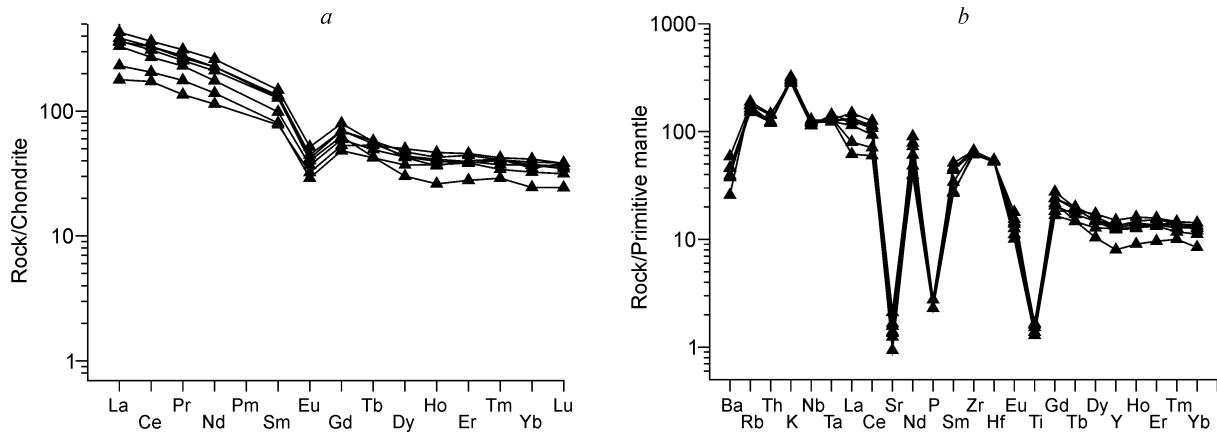
Fig. 8. Chondrite-normalized (Sun and McDonough, 1989) REE patterns (*a*) and primitive-mantle-normalized (Sun and McDonough, 1989) spidergrams (*b*) of rhyolites of the bimodal complex from the Lower Cambrian conglomerates.

HFSE and REE (ppm): $Nb = 81$–92, $Zr = 687$–745, $Hf = 16.2$–16.9, $Ta = 5.05$–5.88, $Zr = 687$–745, $Y = 36$–68, $Th = 10$–12, and $REE = 273$–548, which is also typical of rift-related granites (Table 1), and are poor in TiO_2 (0.28–0.36%) and Sr (19.7–44.4 ppm). The Nb/Y ratio varies from 1.29 to 2.22, i.e., the rocks are enriched in Nb. According to the Y–Nb–Ce diagram (Eby, 1992, 2006) (Fig. 7*f*) they are similar to *A*-type granites with features of oceanic-island basalts (OIB) and continental rift basalts. Their LREE contents are 110–140 times higher and their HREE contents are 20–40 times higher than those in chondrite, and the HREE patterns are gently sloped (Fig. 8*a*). The normative contents of elements decrease from LREE to HREE; the fractionation trend shows $(La/Sm)_n = 2.30$–3.36, $(La/Lu)_n = 4.68$–14.74, and $(La/Yb)_n = 5.60$–19.03. The maximum values are specific for rift-related granites. The REE patterns show a moderate negative Eu anomaly, $(Eu/Eu^*) = 0.44$–0.5, reflecting fractionation of the plagioclase phase. The primitive-mantle-normalized spidergrams (Fig. 8*b*) lack Nb–Ta anomalies (La/Nb $= 0.48$–1.20, the average is 0.90; $(Th/Nb)_{PM} = 0.95$–1.25, the average is 1.07) and show enrichment in all elements and strong negative anomalies of Sr, Ti, and P, which, together with an Eu anomaly, testifies to fractionation of feldspar, apatite, and Fe-Ti oxides. The absence of negative Nb-Ta anomalies rules out a noticeable effect of crustal material on the composition of parental melts. The contents of K are high, whereas Ba and Rb amount to 180–410 and 96–120 ppm, respectively. The content of Sr is extremely low, 20–44 ppm.

Trachybasalts are high-Ti ($TiO_2 = 3.44$–3.79%) tholeiites (Fig. 9*a*) with $SiO_2 = 44.95$–49.74% and $Na_2O + K_2O = 2.18$–4.27 (Fig. 6*a*); the content of Na_2O varies from 1.70 to 3.18%, and the content of K_2O is 0.48 to 2.54%, which is reflected in their ratio, $Na_2O/K_2O = 0.7$–4.1. To minimize the effect of hydrothermal (secondary) processes on the rock composition, classification of the rocks was made using their HFSE ratios and a Zr/TiO_2–Nb/Y diagram (Winchester and Floyd, 1977). According to the latter, the studied rocks are assigned to alkali basalts (Fig. 6*b*). The ratio $Ti/V = 58$–64 also indicates that the rocks are alkali basalts or OIB (Fig. 9*b*). According to the

Zr–Ti–Y and Zr–Nb–Y diagrams (Fig. 9*c*, *d*), they are within-plate alkali basalts. Their REE patterns are similar to those of OIB (Fig. 10*a*). The LREE content is 70–90 times higher and the HREE content is 10 times higher than those in chondrite, and the HREE patterns are gently sloped. The $(La/Lu)_n$ and $(La/Yb)_n$ values vary from 4.90 to 6.03 and from 5.30 to 6.24, respectively. The REE patterns reveal no Eu anomaly, $Eu/Eu^* = 0.86$–1.08. The spidergrams (Fig. 10*b*) show a generally persistent composition, with variations in LILE contents only, as well as positive anomalies of Nb-Ta, Ba, Ti and a weak negative anomaly of Sr.

Trachydolerites are of less stable composition, which might be due to their amygdaloidal structure. In general, the rocks are assigned to high-Ti alkali basalts (trachydolerites, after Oleinikov et al. (1983)). They contain $SiO_2 = 39.20$–49.99% (on average, 44.38%) and $Na_2O + K_2O = 2.29$–4.84% (Fig. 6*a*), with $Na_2O = 1.76$–3.74% and elevated $K_2O = 0.53$–1.38%, which is reflected in their ratio $Na_2O/K_2O = 1.81$–3.98. On the Zr/TiO_2–Nb/Y diagram, the composition points of the rocks lie in the field of alkali basalts or at its boundary with the field of subalkalic basalts (Fig. 6*b*). The rocks are rich in TiO_2, 2.42–4.06% and up to 6.39% in two samples enriched in titanomagnetite and sphene. The ratio $Ti/V = 47$–73 also characterizes them as alkali basalts or OIB (Fig. 9*b*). Their REE pattern is slightly fractionated, with $(La/Lu)_n = 4.06$–6.98 and $(La/Yb)_n = 4.22$–6.78. The REE pattern and spidergrams of the trachydolerites are identical to those of the basalts, which suggests their consanguinity (Fig. 10). The average indicative REE ratios in the trachydolerites and trachybasalts are nearly the same: La/Yb = 7.96 and 8.01, La/Sm = 2.57 and 2.70, Tb/Yb = 0.43 and 0.44, Nb/Y = 0.76 and 0.79, Nb/Zr = 7.9 and 7.9, and Rb/Ba = 0.04 and 0.04, respectively. However, some trachydolerite samples show a weak positive Eu anomaly, $Eu/Eu^* = 0.93$–1.40, a Sr anomaly, and a somewhat wider dispersion of element contents. The content of LREE is 70–90 times higher and the content of HREE is nearly 10 times higher than those in chondrite, and the HREE patterns are gently sloped. In general, the trace-element and REE
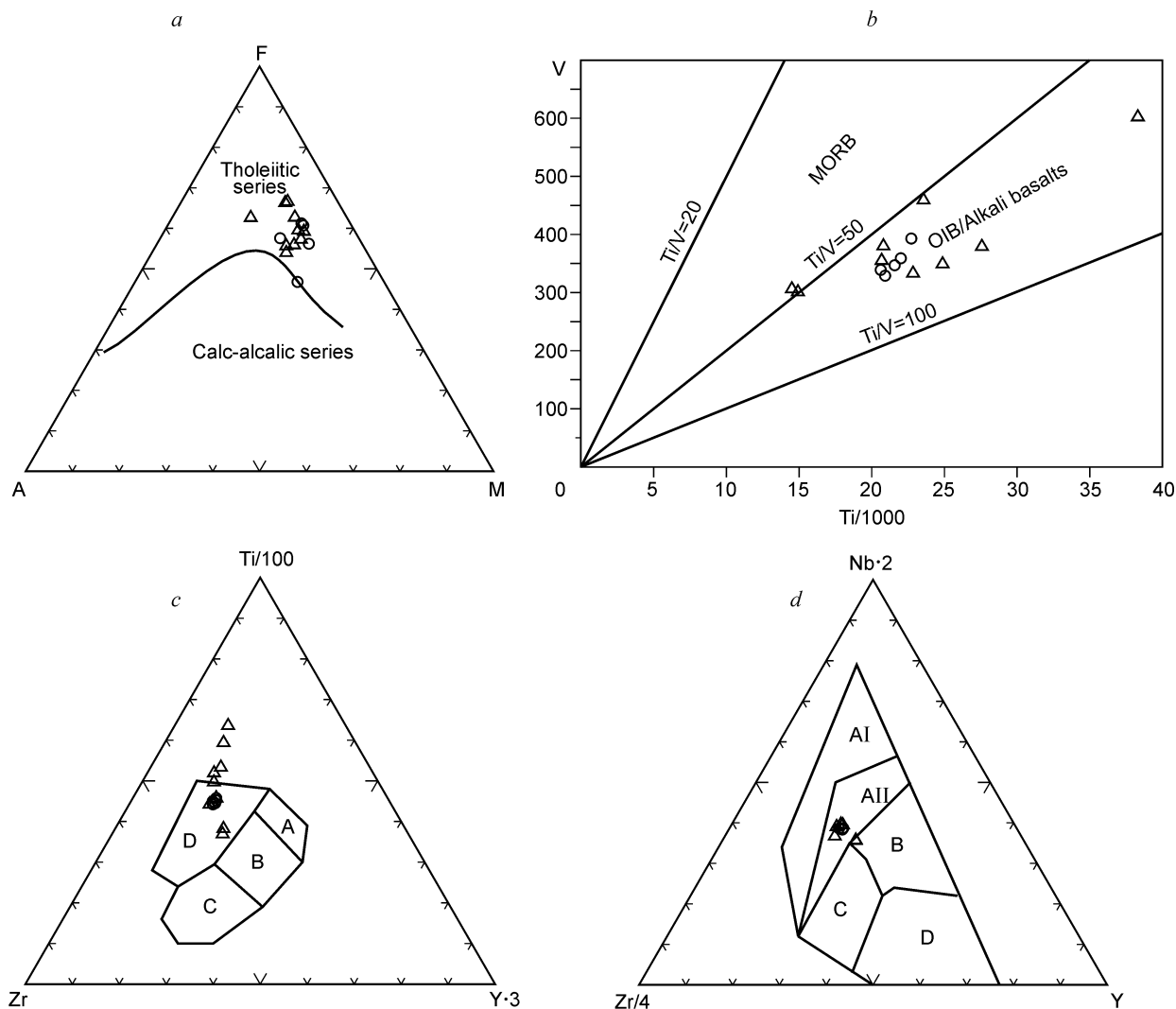
Fig. 9. Geochemical diagrams for trachybasalts and trachydolerites of the bimodal complex. *a*, AFM [(Na$_2$O+K$_2$O)–FeO*–MgO] (Irvine and Baragar, 1971); *b*, V–Ti (Shervais, 1982) (MORB, mid-ocean ridge basalts, OIB, oceanic-island basalts); *c*, Zr–Ti–Y (Pearce and Cann, 1973) (A, island-arc tholeiites; B, MORB, island-arc tholeiites, and calc-alkalic basalts; C, calc-alkalic basalts; D, within-plate basalts); *d*, Zr–Nb–Y (Meschede, 1986) (AI, within-plate alkali basalts, AII, within-plate alkali basalts and within-plate tholeiites; B, *E*-MORB; C, within-plate tholeiites and oceanic-arc basalts; D, *N*-MORB oceanic-arc basalts). Designations follow Fig. 6.

patterns of the trachybasalts are located between the OIB and *E*-MORB trends.

Results of U–Pb isotope studies of rhyolite pebbles from Lower Cambrian conglomerates

Sample 07-AP-41/2. Zircons are present as light brown and transparent euhedral prismatic grains and their fragments and are rich in apatite inclusions as well as melt and fluid inclusions. Some melt inclusions contain silicate glass (up to 20 vol.%). The zircon crystals vary in size from 190 to 300 μm; the elongation coefficient is 1.6–3.0. On CL images, the grain cores are almost nonzonal, whereas the periphery shows a fine sector magmatic zoning (Fig. 11*e*). The content of U varies from 83 to 642 ppm, and the Th/U ratio, from 0.39 to 3.10 (Table 3), which is specific for zircons of magmatic genesis. Two grains with measurement points 6.1

and 9.1 have black cores and gray shells, contain many fluid inclusions, and are the richest in U (393-642 ppm) (Table 3). The concordant age obtained over ten points is 525.6 ± 3.9 Ma, MSWD = 0.000 (Fig. 11*a*).

Sample 07-AP-41/8. Zircons are present as transparent, pinkish, and brownish subeuhedral and euhedral prismatic grains and their fragments and are rich in acicular apatite grains and melt and fluid inclusions. The zircon crystals vary in size from 200 to 450 μm; the elongation coefficient is 1.8–3.1. The CL images of zircons are different (Fig. 11*f*). Crystals with almost black cores and lighter gray coarse-zoned rims (grains with measurement points 1.1, 4.1, and 6.1) are predominant. The grain with measurement point 2.1 is black and intensely reworked by fluids, and the grains with measurement points 3.1 and 7.1 are gray, with clear sector zoning. The zircon with measurement point 6.1 contains many fluid inclusions and has high contents of U (1096 ppm) and Th (921 ppm). Therefore, this grain was ignored during the age
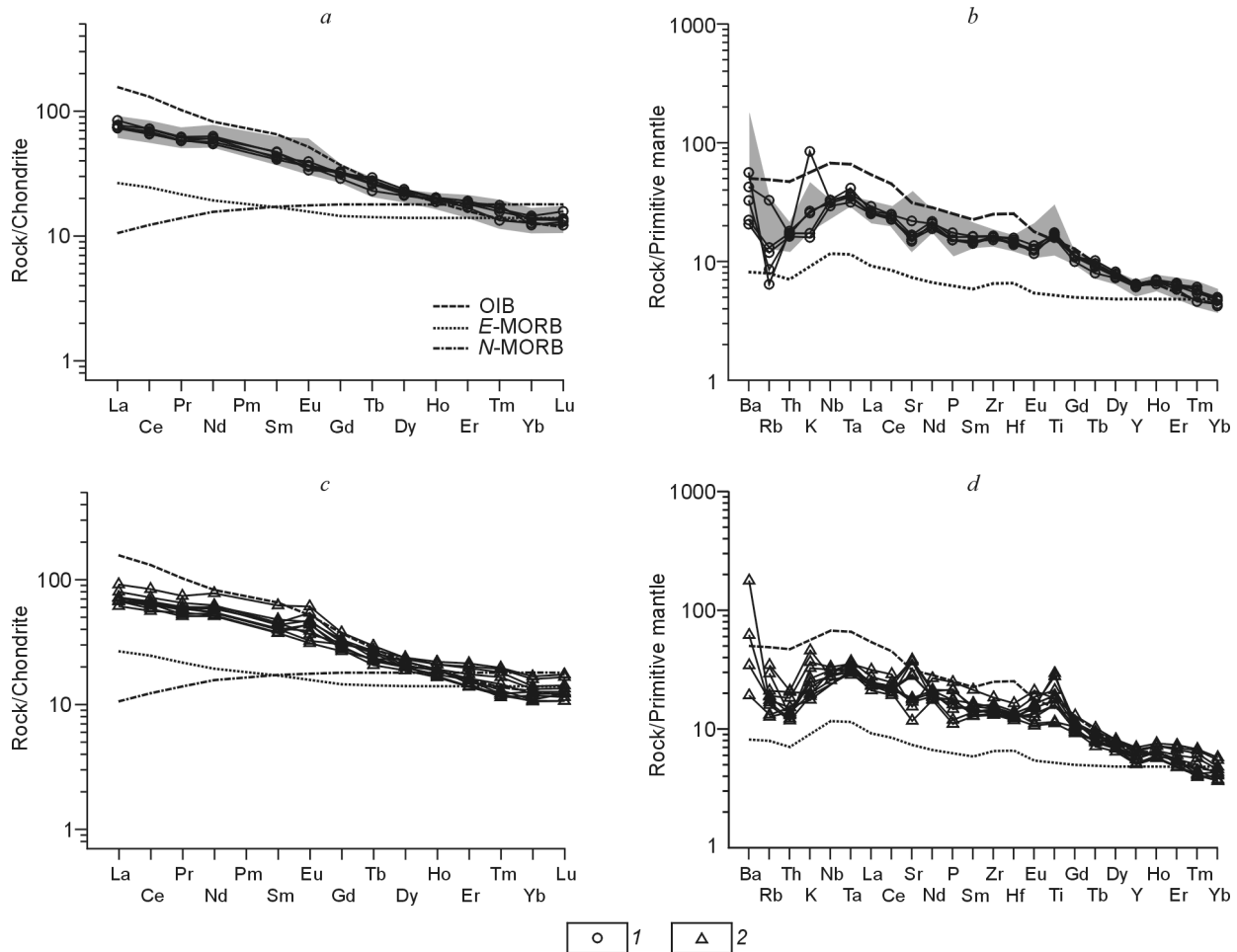
Fig. 10. REE patterns and spidergrams of trachybasalts (*a*, *b*) and trachydolerites (*c*, *d*) of the bimodal complex of the Chekurovka anticline. *1*, trachybasalts; *2*, trachydolerites. Normalized after Sun and McDonough (1989). Gray field in *a* and *b* corresponds to trachydolerites shown in *c* and *d*.

calculation. In the rest zircons, the content of U varies from 44 to 378 ppm, and that of Th, from 36 to 165 ppm; Th/U = 0.38–0.51 (Table 3). The concordant age obtained over nine points is 537.0 ± 4.2 Ma, MSWD = 0.17 (Fig. 11*b*).

Sample 07-AP-41/13. Zircons are present as light brown and transparent euhedral prismatic grains and their fragments, varying in size from 200 to 390 μm; the elongation coefficient is 1.7–2.9. On CL images, the crystals show mostly a fine sector magmatic zoning (Fig. 11*g*). The content of U varies from 27 to 311 ppm, and that of Th, from 10 to 283 ppm, with Th/U = 0.37–1.16 (Table 3), which is typical of zircons of magmatic genesis. The concordant age obtained over 16 points is 546.3 ± 7.7 Ma, MSWD = 0.032 (Fig. 11*c*).

Note that the concordia diagram based on the generalized U–Pb data for the three pebbles yielded a concordant age of 532.6 ± 3.1 Ma (Fig. 11*d*), close to the earlier obtained age of 534.6 ± 0.4 Ma for two pebbles (U–Pb zircon dating, IDTIMS (Bowring et al., 1993)).

Results of Rb-Sr and Sm–Nd isotope studies

We studied the Rb–Sr and Sm–Nd isotope systems in three samples of rhyolites (Tables 4 and 5). Calculations were made

based on the established U–Pb age. The rocks are characterized by abnormally low contents of radiogenic Sr and positive values of $\varepsilon_{Nd}(T)$ (4.2–4.7), which indicates their mantle genesis without the participation of crustal material (Tables 4 and 5, Fig. 12*a*). The high Rb/Sr ratios (2.5–6) permit these rocks to be assigned to highly differentiated *A*-type granites. The $^{87}Rb/^{86}Sr$ value varies from 8.85 to 17.08, whereas the $^{147}Sm/^{144}Nd$ value is relatively constant (0.087–0.093). The Rb–Sr isochron age, determined for the bulk samples, is 538.0 ± 18 Ma ($I_0 = 0.7023 \pm 0.0034$) and agrees with the U–Pb dates even within the high error of calculations. The established similar model ages $T_{Nd}(DM) = 803$–835 Ma and $T_{Nd}(DM)_{2st} = 890$–920 Ma probably reflect the time of separation of the mantle material and its transition into the crust.

The Early Cambrian trachybasalts and underlying trachydolerite sills show very similar Sm–Nd isotope characteristics: The $^{147}Sm/^{144}Nd$ values are within 0.105–0.109 and 0.102–0.111, $\varepsilon_{Nd}(T) = 7.5$–8.9 and 7.2–8.2, $T_{Nd}(DM) = 532$–629 and 577–648 Ma, and $T_{Nd}(DM)_{2st} = 582$–665 and 526–642 Ma, respectively (Table 4). The calculations were made based on the minimum age (525 Ma) of rhyolites from conglomerates underlying the trachybasalts.
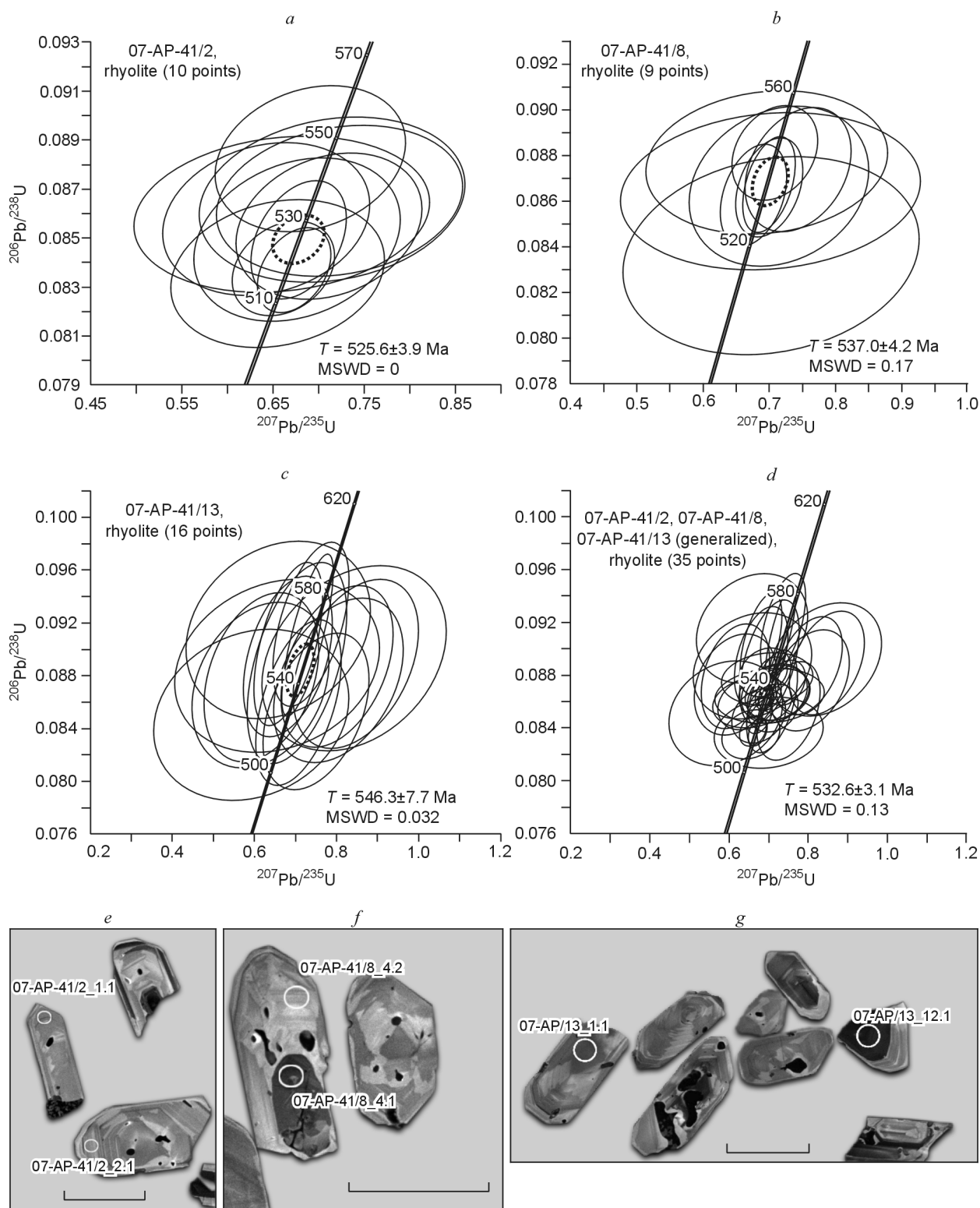
Fig. 11. Concordia diagrams and photomicrographs of zircons from rhyolites of the bimodal complex. *a*, *b*, *c*, For samples 07-AP-41/2, 07-AP-41/8, and 07-AP-41/13, respectively; *d*, common for the three samples; *e*–*g*, photomicrographs of zircons (scalebar is 200 μm) from: *e*, sample 07-AP-41/2, *f*, sample 07-AP-41/8; *g*, sample 07-AP-41/13.

Table 3. Results of U–Pb isotope studies of zircons from rhyolite pebbles of Lower Cambrian conglomerates of the northeastern Siberian Platform

Point	$^{206}Pb_c$ %	U ppm	Th ppm	$\frac{^{232}Th}{^{238}U}$	$^{206}Pb^*$	Age, Ma $\frac{^{206}Pb}{^{238}U}$ (1)	Age, Ma $\frac{^{207}Pb}{^{206}Pb}$ (1)	D %	Total $\frac{^{238}U}{^{206}Pb}$	±%	Total $\frac{^{207}Pb}{^{206}Pb}$	±%	(1) $\frac{^{238}U}{^{206}Pb^*}$	±%	(1) $\frac{^{207}Pb^*}{^{206}Pb^*}$	±%	(1) $\frac{^{207}Pb^*}{^{235}U}$	±%	(1) $\frac{^{206}Pb^*}{^{238}U}$	±%	Error correlation
1	2	3	4	5	6	7	8	9	10		11		12		13		14		15		16
Sample 07-AP-41/2																					
1.1	0.61	108	47	0.45	8.27	544.9±7.2	483±130	–11	11.26	1.3	0.0618	3	11.33	1.4	0.0568	6.1	0.691	6.2	0.0882	1.4	0.222
2.1	0.84	95	36	0.39	7.13	534.8±7.5	625±160	17	11.46	1.4	0.0674	4.3	11.56	1.5	0.0606	7.5	0.723	7.6	0.0865	1.5	0.193
3.1	0.75	93	35	0.39	6.73	517.2±7.4	486±160	–6	11.88	1.4	0.063	3.2	11.97	1.5	0.0569	7.2	0.655	7.4	0.0835	1.5	0.201
4.1	1.19	132	78	0.61	9.85	530.5±7.6	383±160	–28	11.51	1.4	0.0639	2.7	11.65	1.5	0.0543	7.1	0.642	7.3	0.0858	1.5	0.205
5.1	0.57	107	43	0.41	7.85	525.4±8.1	521±150	–1	11.7	1.5	0.0624	3	11.77	1.6	0.0578	6.6	0.676	6.8	0.0849	1.6	0.234
6.1	0.35	393	232	0.61	28.4	518.4±4.7	503±74	–3	11.9	0.92	0.06015	1.6	11.94	0.94	0.0573	3.3	0.661	3.5	0.0837	0.94	0.271
6.2	0.94	83	47	0.59	6.25	535.2±8.1	601±180	12	11.44	1.5	0.0676	3.3	11.55	1.6	0.0599	8.2	0.715	8.3	0.0866	1.6	0.190
7.1	1.47	98	39	0.41	7.37	531.5±7.8	438±220	–18	11.46	1.4	0.0676	3.2	11.63	1.5	0.0556	9.9	0.659	10	0.0859	1.5	0.152
8.1	0.17	172	515	3.10	12.5	525.3±5.8	524±66	0	11.76	1.1	0.0593	2.5	11.78	1.1	0.0579	3	0.677	3.2	0.0849	1.1	0.358
9.1	0.20	642	308	0.50	46.3	518.1±4.2	541±50	4	11.92	0.84	0.0599	1.3	11.95	0.85	0.0583	2.3	0.673	2.4	0.0837	0.85	0.350
10.1	0.80	96	39	0.42	7.11	528.6±7.3	617±120	17	11.6	1.4	0.0669	3.1	11.7	1.4	0.0604	5.7	0.711	5.9	0.0855	1.4	0.243
Measurement error for the standard sample is 0.34%																					
Sample 07-AP-41/8																					
1.1	0.00	369	152	0.43	27.5	536±5.1	550±45	3	11.53	0.99	0.0585	2	11.53	0.99	0.0585	2	0.7	2.3	0.0867	0.99	0.437
1.2	1.18	101	38	0.39	7.58	535.7±8.5	597±160	12	11.4	1.6	0.0695	3	11.53	1.7	0.0598	7.6	0.715	7.8	0.0866	1.7	0.213
2.1	0.37	378	165	0.45	28.7	544.3±5	543±78	0	11.31	0.93	0.0614	1.6	11.35	0.96	0.0584	3.6	0.709	3.7	0.0881	0.96	0.259
3.1	0.95	108	50	0.48	8.24	541.8±7.6	515±230	–5	11.29	1.3	0.0653	6.3	11.4	1.5	0.0576	11	0.697	11	0.0877	1.5	0.136
4.1	0.17	230	113	0.51	17.1	533.3±5.4	488±62	–9	11.57	1.1	0.0583	2.2	11.59	1.1	0.0569	2.8	0.677	3	0.0863	1.1	0.354
4.2	1.58	44	20	0.48	3.18	518±11	636±280	23	11.76	1.9	0.0738	4.4	11.95	2.1	0.0609	13	0.702	13	0.0836	2.1	0.163
5.1	0.31	266	104	0.40	19.9	535.3±5.2	554±61	3	11.51	1	0.0611	2	11.55	1	0.0586	2.8	0.7	3	0.0866	1	0.342
6.1*	1.15	1096	921	0.87	78.9	512.4±4.1	469±78	–9	11.943	0.8	0.06574	1.1	12.08	0.83	0.0564	3.5	0.643	3.6	0.0827	0.83	0.229
6.2	1.16	95	36	0.39	7.15	534.4±8.4	564±290	6	11.43	1.4	0.0684	5.5	11.56	1.6	0.0589	13	0.702	13	0.0864	1.6	0.124
7.1	0.36	130	48	0.38	9.82	539.9±6.6	666±90	23	11.4	1.3	0.0647	2.7	11.45	1.3	0.0618	4.2	0.744	4.4	0.0874	1.3	0.291
Measurement error for the standard sample is 0.34%																					
Sample 07-AP-41/13																					
1.1	0.48	311	110	0.37	24.3	558±15	402±95	–28	11.01	2.8	0.0587	1.9	11.06	2.8	0.0547	4.2	0.682	5.1	0.0904	2.8	0.551
2.1	–	119	81	0.71	8.86	541±15	825±160	52	11.5	2.8	0.0609	2.9	11.42	2.9	0.0666	7.5	0.804	8.1	0.0876	2.9	0.359
3.1	1.16	107	64	0.62	8.48	564±16	296±310	–48	10.8	2.9	0.0618	3.2	10.93	3	0.0522	14	0.659	14	0.0915	3	0.213
4.1	–	218	107	0.51	16.4	548±15	792±130	45	11.39	2.8	0.0573	2.5	11.28	2.8	0.0655	6.4	0.802	7	0.0887	2.8	0.406
5.1	0.72	260	168	0.67	20.1	552±15	426±130	–23	11.1	2.8	0.0613	2.1	11.18	2.8	0.0553	5.9	0.682	6.5	0.0894	2.8	0.427
5.2	1.06	100	59	0.61	7.67	548±16	360±340	–34	11.15	2.9	0.0624	3.2	11.27	3	0.0537	15	0.66	15	0.0887	3	0.197
6.1	1.61	79	31	0.41	5.87	526±16	216±370	–59	11.56	3	0.0637	3.6	11.75	3.1	0.0505	16	0.592	16	0.0851	3.1	0.190
7.1	–	108	59	0.56	8.15	549±15	905±140	65	11.36	2.9	0.0617	3.3	11.25	2.9	0.0692	6.8	0.848	7.4	0.0889	2.9	0.399
7.2	–	266	162	0.63	20.8	562±15	537±47	–4	10.99	2.8	0.0579	2.1	10.99	2.8	0.0582	2.2	0.73	3.5	0.091	2.8	0.788
8.1	0.00	27	10	0.39	2.04	550±18	507±130	–8	11.24	3.5	0.0574	6.1	11.24	3.5	0.0574	6.1	0.704	7.1	0.089	3.5	0.497
9.1	–	252	283	1.16	18.4	528±14	736±130	39	11.78	2.8	0.0602	3.2	11.73	2.9	0.0638	6.4	0.751	7	0.0853	2.9	0.410
10.1	0.33	304	188	0.64	24.1	566±15	540±92	–5	10.86	2.8	0.0609	3.5	10.89	2.8	0.0583	4.2	0.737	5.1	0.0918	2.8	0.548
11.1	0.82	94	37	0.41	7.17	543±16	234±200	–57	11.29	2.9	0.0576	3.6	11.38	3	0.0509	8.8	0.616	9.3	0.0879	3	0.322
12.1	–	95	37	0.41	7.15	551±17	887±220	61	11.38	3.1	0.0565	3.6	11.21	3.2	0.0686	11	0.844	11	0.0892	3.2	0.292
13.1	0.64	173	86	0.51	13.1	540±15	251±250	–53	11.38	2.9	0.0565	3	11.45	2.9	0.0512	11	0.617	11	0.0873	2.9	0.264
14.1	0.26	95	40	0.43	7.06	532±15	596±110	12	11.6	3	0.0619	3.6	11.63	3	0.0598	5.1	0.709	5.9	0.086	3	0.500
Measurement error for the standard sample is 0.98%																					

Note. Measurement errors are at the level 1σ; Pb_c and Pb^*—portions of common and radiogenic lead, respectively; (1), correction for common lead was made after ^{204}Pb; D, discordance.

* Grain 6.1 was ignored on the construction of a concordia diagram.

Table 4. Results of Sm–Nd isotope studies of rocks of the bimodal complex of the Chekurovka anticline

Sample	Age, Ma	Sm	Nd	$^{147}Sm/^{144}Nd$	$^{143}Nd/^{144}Nd$	$\pm 2\sigma$	$\varepsilon_{Nd}(0)$	$\varepsilon_{Nd}(T)$	$T(DM)$	$T(DM\text{-}2)$
Rhyolite pebbles in Lower Cambrian conglomerates										
07-AP-41/2	532	10.2	71.2	0.0869	0.512474	0.000003	–3.2	4.2	815	914
07-AP-41/8	532	16.6	107.7	0.0933	0.512492	0.000003	–2.8	4.3	835	920
07-AP-41/13	532	12.5	85.7	0.0880	0.512490	0.000001	–2.9	4.7	803	890
Early Cambrian trachybasalts										
07-AP-44	525	4.7	27.2	0.1054	0.512774	0.000002	2.7	8.8	532	533
09-AP-88/1	525	5.2	29.2	0.1077	0.512786	0.000003	2.9	8.9	526	526
09-AP-104/1	525	5.0	27.6	0.1086	0.512718	0.000003	1.6	7.5	629	642
Early Cambrian (?) trachydolerite sills and dikes in Neoproterozoic deposits										
09-AP-102/1	525	4.8	27.3	0.1072	0.512699	0.000001	1.2	7.2	648	665
07-AP-40	525	5.0	27.3	0.1113	0.512764	0.000002	2.5	8.2	577	582
09-AP-120/1	525	5.3	31.3	0.1016	0.512692	0.000002	1.1	7.4	625	645

Table 5. Results of Rb–Sr isotope studies of rocks of the bimodal complex of the Chekurovka anticline

Sample	Age, Ma	^{87}Rb	^{86}Sr	$^{87}Rb/^{86}Sr$	$^{87}Sr/^{86}Sr$	Error correlation	$(^{87}Sr/^{86}Sr)i$	$\varepsilon_{Sr}(T)$
Rhyolite pebbles in Lower Cambrian conglomerates								
07-AP-41/2	532	36.5222	2.1134	17.0825	0.83300	5	0.70346	–6
07-AP-41/8	532	31.5222	3.5209	8.8499	0.76920	5	0.70209	–25
07-AP-41/13	532	33.2365	3.0702	10.701	0.78560	4	0.70445	8
Early Cambrian trachybasalts								
07-AP-44	525	2.3324	35.8935	0.0642	0.70710	4	0.70662	39
09-AP-88/1	525	2.4233	37.6003	0.0637	0.70740	4	0.70692	43
09-AP-104/1	525	1.1203	32.6110	0.0340	0.70750	4	0.70725	48

In general, the $\varepsilon_{Nd}(T)$ value of the basites is much higher than that of the rhyolites and is close to the $\varepsilon_{Nd}(T)$ value of N-MORB (Khudoley et al., 2013). However, all trachybasalt samples are rich in radiogenic Sr, with $I_0 = 0.7066$–0.7073 (Table 5) typical of continental crust.

Discussion

Peculiarities of the studied igneous rock complex. The above-considered rock association is characterized by a distinct bimodal composition and high alkalinity. According to available geological data, the bimodal complex had an antidrome evolution. Both the felsic and mafic rocks are of within-plate genesis, and the trachyrhyolites correspond in geochemical features to A-type granites. The high contents of Ta, Nb, Hf, Tb, and Zr are usually indicators of the presence of enriched mantle material in the magmatic sources of the rocks. In proportions of Y, Nb, and Ce they correspond to A-type granites with characteristics of OIB and continental-rift basalts and can be interpreted as products of basaltic magma of within-plate settings or as rocks of mantle genesis (Hocker

et al., 2005). The isotopic composition of the rocks under study is characterized by high positive ε_{Nd} and elevated I_0 values in the basalts and by low (mantle) I_0 values in the rhyolites. We have revealed neither geochemical nor isotope evidence for significant contamination of the rhyolites with continental-crust material. Their geochemical characteristics suggest mantle sources. The basalts that underwent hydrothermal alterations are enriched in radiogenic Sr (Fig. 12a, Table 5). The similar isotope compositions of the studied rocks, the geochemical characteristics of salic rocks of the bimodal association inherited by them, and the small amount of felsic rocks as compared with that of trachybasalts led us to the conclusion that the trachyrhyolite melts might have been the product of deep differentiation of mantle trachybasaltic magmas.

The Sm/Yb ratio can be used to estimate the depth of melting, as it is insensitive to fractional crystallization (McKenzie and O'nions, 1991). On the Sm/Yb–La/Yb diagram (Fig. 12b), the composition points of basites (as well as rhyolites) are arranged near the melting curve for garnet-containing peridotite. The absence of negative Nb–Ta anomalies rules out a significant influence of crustal material on the
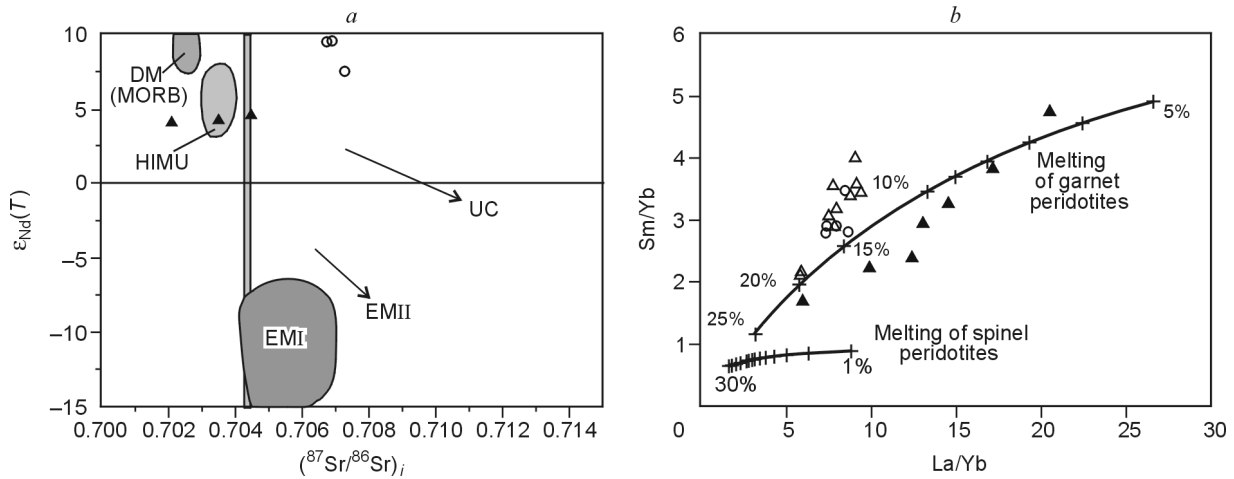
Fig. 12. ε_{Nd}–$(^{87}Sr/^{86}Sr)_i$ diagram (major mantle components, after Zindler and Hart (1986)) (a) and Sm/Yb–La/Yb diagram (Chen et al., 2013) (b) for the Early Cambrian rocks of the bimodal complex of the Chekurovka anticline core. Designations follow Fig. 6.

composition of parental melts. The lower degree of enrichment of the basites relative to OIB might be due to the involvement of garnet in the melting (Khudoley et al., 2013). As mentioned above, the trachybasalts show features of N-MORB (high positive $\varepsilon_{Nd}(T)$ values), and high $(Tb/Yb)_{PM}$ ratios evidence that the rocks melted out of the garnet-containing peridotitic mantle at depths of >90 km, with the low degree of melting of the latter (Khudoley et al., 2013). On the $(Th/Yb)_{PM}$–$(Nb/Yb)_{PM}$ diagram, the basites fall in the field of mantle melts, and the rhyolites, despite the higher ratios of these elements (0.28–0.38), are localized near the upper boundary of this field (Fig. 13). The Th/Yb ratio is the most sensitive to the presence of garnet in the source; at the same time, it varies little during magma fractionation (MacDonald et al., 2001; Wang et al., 2002). The studied basites are characterized by Tb/Yb = 0.36–0.52 and La/Yb = 5.89–9.45, which corresponds to the field of melting of the garnet-containing (~1% garnet in restite) fertile lherzolitic mantle (MacDonald et al., 2001). As seen from the $(Th/Yb)_{PM}$–$(La/Sm)_{PM}$ diagram, the underlying trachydolerites have similar characteristics (Fig. 14). Their contents of trace and rare-earth elements indicate that the rocks formed from melts intermediate in composition between OIB and E-MORB (Fig. 10), with a noticeable positive Ti anomaly, which is, most likely, a specific feature of these magmas. At the same time, the high positive values of $\varepsilon_{Nd}(T)$ (7.5–8.9) suggest that the parental melts were generated from a depleted source and negligibly interacted with continental-crust material. The high $(Nb/Yb)_{PM}$ ratio suggests mixing of magmas generated from enriched and depleted mantle sources. Mafic magmas might have been produced from a heterogeneous source or have interacted with the depleted mantle before their intrusion (Khudoley et al., 2013).

Thus, the proximal occurrence and close ages of rocks of the bimodal complex, the assignment of the trachyrhyolites to A–type granites, and the similarity in geochemical features between the rocks of the basalt flow overlying the rhyolites and the trachydolerites of associated sills and dikes testify to

their close temporal and spatial occurrence in the extension (presumably, of rift nature) setting.

The age of rocks. The concordant ages of zircons from two pebbles, 525.6 ± 3.9 and 537.0 ± 4.2 Ma (U–Pb dating), point to the crystallization of subvolcanic rhyolites in the Early Cambrian; moreover, the second date is close to the earlier estimated age of 534.6 ± 0.4 Ma (Bowring et al., 1993). The concordant age of rhyolites from the third pebble is 546.0 ± 7.7 Ma, which indicates (with regard to the error of calculation) their Late Vendian–Early Cambrian age.

Thus, the obtained data suggest that the trachyrhyolite complex began to form either in the late Vendian or at the Vendian–Cambrian boundary or in the earliest Cambrian but no later than at 538 Ma (the minimum age of rhyolites from the third pebble, with regard to the error of calculation). We
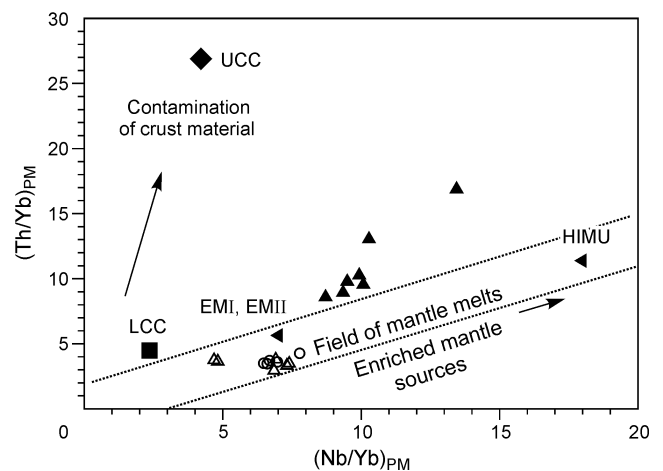

Fig. 13. Primitive-mantle-normalized (Sun and McDonough, 1989) $(Th/Yb)_{PM}$–$(Nb/Yb)_{PM}$ diagram for the Early Cambrian rocks of the bimodal complex of the Chekurovka anticline. UCC, upper continental crust, LCC, lower continental crust (Taylor and McLennan, 1985); enriched mantle (EMI, EMII) and HIMU (high value of $\mu = {}^{238}U/{}^{204}U$) (Condie, 2001). Composition points of basalts are given after Khudoley et al. (2013). Designations follow Fig. 6.
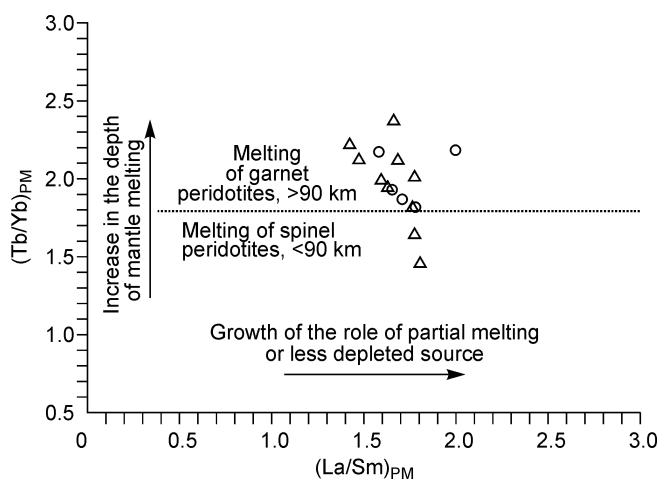
Fig. 14. Primitive-mantle-normalized (Sun and McDonough, 1989) $(Tb/Yb)_{PM}$–$(La/Sm)_{PM}$ diagram of trachybasalts and trachydolerites of the bimodal complex of the Chekurovka anticline. Discriminant line separating the sources of magma is drawn after Wang et al. (2002). Composition points of basalts are given after Khudoley et al. (2013). Designations follow Fig. 6.

estimated that the intrusion of subvolcanic trachyrhyolites was completed no earlier than 525 Ma. The basalts overlying the rhyolites and the trachydolerites in Neoproterozoic deposits formed, apparently, at the same time or somewhat later.

Unfortunately, despite the large number of analyzed zircons (16 grains), the oldest age of the trachyrhyolites was estimated with a great error. It is close to the age of pyroclastic breccia in the Olenek Uplift, determined by Bowring et al. (1993), 543.9 ± 0.24 Ma (U–Pb zircon dating). This breccia occurs in the base of the Cambrian strata and is separated from the top of the Vendian strata by a 8 m thick bed of conglomerates and sandstones. In the studied section, trachyrhyolites and trachybasalts rest upon 15 m thick sandstones overlying Vendian deposits, as in the Olenek Uplift; their accumulation took a particular time. The age of the Neoproterozoic–Cambrian boundary is now accepted as 541.0 Ma (Gradstein et al., 2012). If admitting that the trachyrhyolites began to form just after the accumulation of sandstones, the Neoproterozoic–Cambrian boundary might be older. Of course, this hypothesis calls for additional studies.

There is one more possible scenario. Trachyrhyolites intruded in the immediate vicinity of the study area, on the eastern slope of the Olenek Uplift, throughout the Late Vendian–early Early Cambrian (Fortunian Age (Gradstein et al., 2012)) and underwent erosion and deposition as conglomerates only in the late Terreneuvian (Gradstein et al., 2012).

As an alternative, we can admit that the intermediate magma chamber was located at a great depth during the formation of the bimodal complex and that crystallization of zircons in it started in the Late Vendian (or at the Vendian–Cambrian boundary) and was completed after the ascent of the melts to the hypabyssal level in the early Early Cambrian. This is suggested from the presence of melt inclusions in zircons of different degrees of crystallization: Small round, totally crystalline inclusions free of a visible fluid phase are

specific for mantle rocks, whereas large, often shapeless inclusions with a silicate glass phase, ore minerals, and, often, a fluid phase are typical of shallow-depth rocks.

Conclusions

At the Vendian–Early Cambrian, continental rifting accompanied by bimodal antidrome magmatism took place in the northeastern Siberian Platform. First, hypabyssal trachyrhyolites similar to anorogenic granites formed, which were then eroded and deposited as conglomerates. These subvolcanoes were not revealed, but they might be present west of the Chekurovka anticline, in the eastern slope of the Olenek Uplift, where they might be overlain by Phanerozoic deposits. Then, the eruption of trachybasalts took place, and a thick intrusive complex of dolerite sills and dikes formed at a depth. There are no igneous bodies above these Early Cambrian basalts. According to geochemical data, these rocks, like the abundant intrusive dolerite sills and dikes in the lower Neoproterozoic deposits, are within-plate alkali basalts and tholeiites. Our petrogeochemical and isotope data further support the Early Cambrian age of the whole basic rock complex exposed in the study area (Khudoley et al., 2013; Kiselev et al., 2012a,b; Prokopiev et al., 2011).

In the late Vendian–early Cambrian, the eastern (hereafter, in the modern frame of reference) margin of the Siberian Craton was affected by rifting. Evidence of this process was found in the southeast of the Craton (Khudoley, 2003; Khudoley and Guriev, 2003), in the north of the Omolon and Kolyma terranes (Bulgakova, 1991, 1996; Tkachenko, 1994), in the north of the Omulevka terrane (Karyakin and Oxman, 1999), and in the northeast of the Siberian Craton (Bulgakova, 1996; Khudoley, 2003; Pelechaty, 1996; Pelechaty et al., 1996) (Fig. 15). According to some modern paleotectonic reconstructions, this part of the Siberian Craton might have been connected with the eastern margin of Laurentia in the Late Neoproterozoic (Late Riphean–Late Vendian) (Sears, 2012; Sears and Price, 2003), and continental rifting that started at the Vendian–Cambrian boundary and was accompanied by the formation of a bimodal complex in the northeast of the Siberian Craton resulted in their separation.

The obtained isotope-geochronological data suggest that the formation of the bimodal complex began at the Vendian–Cambrian boundary and terminated no earlier than the Terreneuvian Epoch (Tommotian), i.e., lasted 20 Myr. This agrees with the age of the synrift phase of evolution of the Vendian–Cambrian sedimentary basin which was recognized in the northeastern Siberian Craton (Pelechaty et al., 1996).
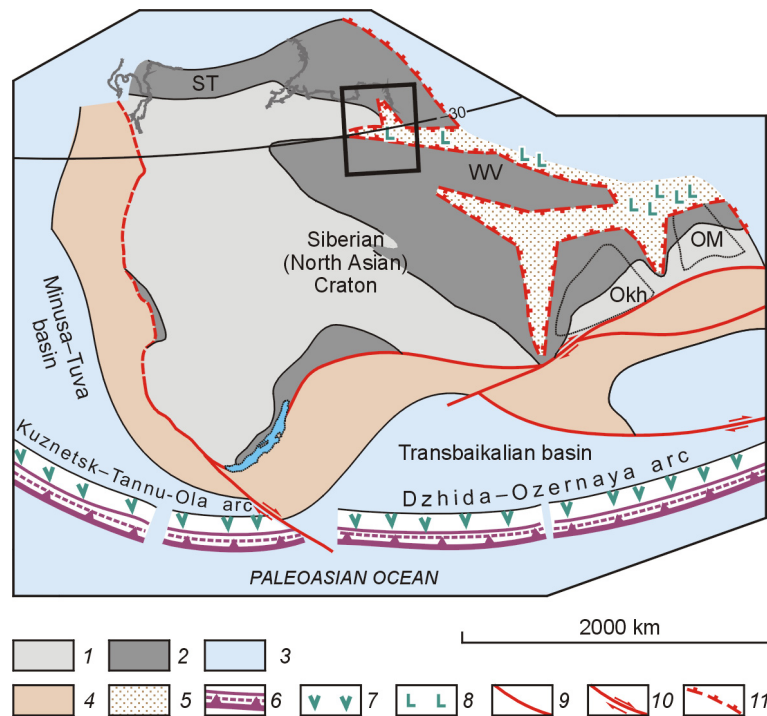
Fig. 15. Paleotectonic reconstruction for the Early Cambrian, after Berzin et al. (2010) and Parfenov et al. (2003), with modifications and supplements. *1*, craton (OKh, Okhotsk terrane; OM, Omolon terrane); *2*, passive continental margins and epicontinental seas (ST, South Taimyr; WV, West Verkhoyansk); *3*, oceanic crust; *4*, collage of accreted terranes; *5*, rift-related sedimentary basins; *6*, subduction zone and accretionary wedge; *7*, suprasubductional magmatic arcs; *8*, rift-related bimodal volcanic and plutonic rocks; *9*, faults; *10*, strike-slip faults; *11*, normal faults. Rectangle marks the study area.

References

Berzin, N.A., Distanov, E.G., Tomurtogoo, O., Prokopiev, A.V., Timofeev, V.F., Nokleberg, W.J., 2010. Chapter 5. Neoproterozoic through Silurian metallogenesis and tectonics of Northeast Asia, in: Nokleberg, W.J. (Ed.), Metallogenesis and Tectonics of Northeast Asia. U.S. Geological Survey Professional Paper 1765, pp. 5-1–5-71.

Black, L.P., Kamo, S.L., Allen, C.M., Heinikoff, J.N., Davis, D.W., Russel, J., Korsch, R.J., Foudonlis, C., 2003. TEMORA 1: a new zircon standard for U–Pb geochronology. Chem. Geol. 200, 155–170.

Bowring, S.A., Grotzinger, J.P., Isachsen, C.E., Knoll, A.H., Pelechaty, Sh.M., Kolosov, P., 1993. Calibrating rates of Early Cambrian evolution. Science 261, 1293–1298.

Bulgakova, M.D., 1991. The Early–Middle Paleozoic Unit of the Northeastern USSR (Sedimentological Analysis) [in Russian]. YaNTs SO AN SSSR, Yakutsk.

Bulgakova, M.D., 1996. Paleogeography of Yakutia in the Early–Middle Paleozoic [in Russian]. YaNTs SO RAN, Yakutsk.

Chen, X., Liangshu Shu, Santosh, M., Xixi Zhao, 2013. Island arc-type bimodal magmatism in the eastern Tianshan Belt, Northwest China: geochemistry, zircon U–Pb geochronology and implications for the Paleozoic crustal evolution in Central Asia. Lithos 168–169, 48–66.

Condie, K.C., 2001. Mantle Plumes and Their Record in Earth History. Cambridge University Press, Oxford, UK.

Dobretsov, N.L., 2003. Mantle plumes and their role in the formation of anorogenic granitoids. Geologiya i Geofizika (Russian Geology and Geophysics) 44 (12), 1243–1251 (1199–1218).

Dobretsov, N.L., 2010. Global geodynamic evolution of the earth and global geodynamic models. Russian Geology and Geophysics (Geologiya i Geofizika) 51 (6), 592–610 (761–784).

Dobretsov, N.L., 2011. Early Paleozoic tectonics and geodynamics of Central Asia: role of mantle plumes. Russian Geology and Geophysics (Geologiya i Geofizika) 52 (12), 1539–1552 (1957–1973).

Dobretsov, N.L., Vernikovsky, V.A., 2001. Mantle plumes and their geologic manifestation. Int. Geol. Rev. 43 (9), 771–787.

Dobretsov, N.L., Buslov, M.M., Vernikovsky, V.A., 2003. Neoproterozoic to Early Ordovician evolution of the Paleo-Asian Ocean: implications to the break-up of Rodinia. Gondwana Res. 6(2), 143–159.

Eby, G.N., 1992. Chemical subdivision of the *A*-type granitoids: petrogenetic and tectonic implications. Geology 20, 641–644.

Eby, G.N., 2006. Distinctions between *A*-type granites and petrogenetic pathways, in: Symposium on Magmatism, Crustal Evolution, and Metallogenesis of the Amazonian Craton. Abstracts Volume and Field Trips Guide. Belém, PRONEX-UFPA/SBG-NO, p. 48.

Frost, B.R., Frost, C.D., 2008. A geochemical classification for feldspathic rocks. J. Petrol. 49 (11), 1955–1969.

Frost, B.R., Arculus, R.J., Barnes, C.G., Collins, W.J., Ellis, D.J., Frost, C.D., 2001. A geochemical classification for granitic rock suites. J. Petrol. 42, 2033–2048.

Goldstein, S.J., Jacobsen, S.B., 1988. Nd and Sr isotopic systematics of river water suspended material: implications for crustal evolution. Earth Planet. Sci. Lett. 87, 249–265.

Gradstein, F.M., Ogg, J.G., Schmitz, M.D., Ogg, G.M., 2012. The Geologic Time Scale 2012. Elsevier, Oxford, UK.

Hocker, S.M., Thurston, P.C., Gibson, H.L., 2005. Volcanic stratigraphy and controls on mineralization in the Genex Mine area, Kamiskotia area: Discover Abitibi initiative; Ontario Geological Survey, Open File Report 6156.

Irvine, T.N., Baragar, W.R.A., 1971. A guide to the chemical classification of the common volcanic rocks. Canad. J. Earth Sci. 8, 523–548.

Jacobsen, S.B., Wasserburg, G.J., 1984. Sm–Nd evolution of chondrites and achondrites, II. Earth Planet. Sci. Lett. 67, 137–150.

Karyakin, Yu.V., Oxman, V.S., 1999. Early Paleozoic volcanosedimentary deposits of the Selennyakh block and their geodynamic nature, in: Geology and Tectonics of Platforms and Orogenic Areas of Northeastern Asia. Proceedings of the Meeting [in Russian]. YaNTs SO RAN, Yakutsk, Vol. 1, pp. 83–87.

Khabarov, E.M., Izokh, O.P., 2014. Sedimentology and isotope geochemistry of Riphean carbonates in the Kharaulakh Range of northern East Siberia. Russian Geology and Geophysics (Geologiya i Geofizika) 55 (5/6), 629–648 (797–820).

Khudoley, A.K., 2003. Tectonics of the Passive Margins of Ancient Continents (by the Example of the Eastern Margin of the Siberian Platform and Western Margin of the North American Platform). ScD Thesis [in Russian]. GIN RAN, Moscow.

Khudoley, A.K., Guriev, G.A., 2003. Influence of syn–sedimentary faults on orogenic structure: examples from the Neoproterozoic–Mesozoic East Siberian passive margin. Tectonophysics 365, 23–43.

Khudoley, A.K., Prokopiev, A.V., Chamberlain, K.R., Ernst, R.E., Jowitt, S.M., Malyshev, S.V., Zaitsev, A.I., Kropachev, A.P., Koroleva, O.V., 2013. Early Paleozoic mafic magmatic events on the eastern margin of the Siberian Craton. Lithos 174, 44–56.

Khudoley, A., Chamberlain, K., Ershova, V., Sears, J., Prokopiev, A., MacLean, J., Kazakova, G., Malyshev, S., Molchanov, A., Kullerud, K., Toro, J., Miller, E., Veselovskiy, R., Li, A., Chipley, D., 2015. Proterozoic supercontinental restorations: Constraints from provenance studies of Mesoproterozoic to Cambrian clastic rocks, eastern Siberian Craton. Precambrian Res. 259, 78–94.

Kiselev, A.I., Yarmolyuk, V.V., Kolodeznikov, I.I., Struchkov, K.K., Egorov, K.N., 2012a. The northeastern boundary of the Siberian Craton and its formation peculiarities (derived from occurrences of Early Cambrian and Devonian intraplate magmatism). Dokl. Earth Sci. 447 (1), 1252–1258.

Kiselev, A.I., Yarmolyuk, V.V., Kolodeznikov, I.I., Struchkov, K.K., Egorov, K.N., 2012b. Lower Cambrian and Devonian intraplate magmatism on the northeastern margin of the Siberian Craton, in: Geodynamic Evolution of Lithosphere of the Central Asian Mobile Belt (from Ocean to Continent). Proceedings of the Meeting [in Russian]. IZK SO RAN, Irkutsk, Vol. 1, pp. 103–105.

Kolodeznikov, I.I., Struchkov, K.K., 2001. Magmatism of the Kharaulakh [in Russian]. Yakutskii Universitet, Yakutsk.

Kolodeznikov, I.I., Krutii, V.M., Mel'nikov, A.V., Menner, V.V., 1974. Pre-Upper Paleozoic Kharaulakh lavas, in: Issues of Applied Physics [in Russian]. Yakutskii Universitet, Yakutsk, pp. 99–111.

Kotov, A.B., Kovach, V.P., Sal'nikova, E.B., Glebovitskii, V.A., Yakovleva, S.Z., Berezhnaya, N.G., Myskova, T.A., 1995. Stages of formation of continental crust in the center of the Aldan granulite-gneiss area: U–Pb and Sm-Nd isotope data on granitoids. Petrologiya 3 (1), 99–100.

Kuzmin, M.I., Yarmolyuk, V.V., Kravchinsky, V.A., 2010. Phanerozoic hot spot traces and paleogeographic reconstructions of the Siberian continent based on interaction with the African large low shear velocity province. Earth Sci. Rev. 102, 29–59.

Le Bas, M.J., Le Maitre, R.W., Streckeisen, A., Zanettin, B., 1986. A chemical classification of volcanic rocks based on the total alkali–silica diagram. J. Petrol. 27, 745–750.

Leonov, B.N., Gogina, N.I., 1968. Early Paleozoic volcanism in the northeastern Siberian Platform. Sovetskaya Geologiya, No. 4, 94-102.

Liew, T.C., Hofmann, A.W., 1988. Precambrian crustal components, plutonic associations, plate environment of the Hercynian Fold Belt of Central Europe: Indications from a Nd and Sr isotopic study. Contrib. Mineral. Petrol. 98, 129–138.

Ludwig, K.R., 2001. SQUID 1.02. A User's Manual. Berkeley Geochronology Center Special Publication, No. 2, 2455 Ridge Road, Berkeley, CA 94709, USA.

Ludwig, K.R., 2003. ISOPLOT 3.00. A User's Manual. Berkeley Geochronology Center Special Publication, No. 4, 2455 Ridge Road, Berkeley, CA 94709, USA.

MacDonald, R., Rogers, N.W., Fitton, J.G., 2001. Plume–lithosphere interactions in the generation of the basalts of the Kenya rift, East Africa. J. Petrol. 42 (5), 877–900.

Maniar, P.D., Piccoli, P.M., 1989. Tectonic discrimination of granitoids. Geol. Soc. Am. Bull. 101, 635–643.

McKenzie, D.A.N., O'nions, R.K., 1991. Partial melt distributions from inversion of rare earth element concentrations. J. Petrol. 32, 1021–1091.

Meschede, M., 1986. A method of discriminating between different type of Middle ocean ridge basalts and continental tholeiites with the Nb–Zr–Y diagram. Chem. Geol. 56, 207–218.

Missarzhevskii, V.V., 1989. The Most Ancient Skeleton Fossils and Stratigraphy of the Precambrian-Cambrian Boundary Deposits [in Russian]. Nauka, Moscow.

Nakhabtsev, Yu.S., Dukart, Yu.A., Korchagin, V.P., Shikhorina, N.M., 1971. Cambrian trap formation of the Siberian Platform. Doklady AN SSSR 201 (1), 166–168.

Oleinikov, B.V., Mashchak, M.S., Kolodeznikov, I.I., Kopylova, A.G., Savinov, V.T., Tomshin, M.D., Tulasynov, B.N., 1983. Petrology and Geochemistry of Late Precambrian Intrusive Basites of the Siberian Platform [in Russian]. Nauka, Novosibirsk.

Parfenov, L.M., Berzin, N.A., Khanchuk, A.I., Badarch, G., Belichenko, V.G., Bulgatov, A.N., Dril', S.I., Kirillova, G.L., Kuz'min, M.I., Nokleberg, W., Prokopiev, A.V., Timofeev, V.F., Tomurtogoo, O., Yan, H., 2003. Model for the formation of orogenic belts of Central and Northeastern Asia. Tikhookeanskaya Geologiya, No. 6, 7–42.

Pearce, J.A., Cann, J.R., 1973. Tectonic setting of basic volcanic rocks determined using trace element analyses. Earth Planet. Sci. Lett. 19, 290–300.

Pearce, J.A., Harris, N.B.W., Tindle, A.G., 1984. Trace element discrimination diagrams for the tectonic interpretation of granitic rocks. J. Petrol. 25, 956–983.

Pelechaty, Sh.M., 1996. Stratigraphic evidence for the Siberia–Laurentia connection and Early Cambrian rifting. Geology 24, 719–722.

Pelechaty, Sh.M., Grotzinger, J.P., Kashirtsev, V.A., Zhernovsky, V.P., 1996. Chemostratigraphic and sequence stratigraphic constraints on Vendian–Cambrian basin dynamics, Northeast Siberian Craton. J. Geol. 104, 543–563.

Prokopiev, A.V., Deikunenko, A.V., 2001. Deformation structures of fold-thrust belts, in: Parfenov, L.M., Kuz'min, M.I. (Eds.), Tectonics, Geodynamics, and Metallogeny of the Sakha Republic (Yakutia) [in Russian]. Nauka/Interperiodika, Moscow, pp. 156–198.

Prokopiev, A.V., Parfenov, L.M., Tomshin, M.D., Kolodeznikov, I.I., 2001. The Cover of the Siberian Platform and adjacent fold-and-thrust belts, in: Parfenov, L.M., Kuz'min, M.I. (Eds.), Tectonics, Geodynamics, and Metallogeny of the Sakha Republic (Yakutia) [in Russian]. Nauka/Interperiodika, Moscow, pp. 113–146.

Prokopiev, A.V., Khudoley, A.K., Roev, S.P., Kazakova, G.G., Lokhov, D.K., Koroleva, O.V., Ershova, V.B., Sergeev, S.A., 2011. New data on the Early Cambrian bimodal volcanism in the northeastern Siberian platform, in: Large Igneous Provinces of Asia: Mantle Plumes and Metallogeny. Petrographica, Irkutsk, pp. 196–199.

Repina, L.N., Lazarenko, N.P., Meshkova, N.P., Korshunov, V.I., Nikiforov, N.I., Aksarina, N.A., 1974. Lower Cambrian Biostratigraphy and Fauna of Kharaulakh (Tuora-Sis Ridge) [in Russian]. IGiG SO AN SSSR, Novosibirsk.

Sears, J.W., 2012. Transforming Siberia along the Laurussian margin. Geology 40, 535–538.

Sears, J.W., Price, R.A., 2003. Tightening the Siberian connection to western Laurentia. Geol. Soc. Am. Bull. 115, 943–953.

Semikhatov, M.A., Serebryakov, S.N., 1983. The Riphean Hypostratotype of Siberia [in Russian]. Nauka, Moscow.

Shervais, J.W., 1982. Ti–V plots and the petrogenesis of modern and ophiolitic lavas. Earth Planet. Sci. Lett. 59, 101–118.

Shpunt, B.R., 1987. Late Precambrian Rifting of the Siberian Platform [in Russian]. YaF SO AN SSSR, Yakutsk.

Shpunt, B.R., Oleinikov, B.V., 1989. Late Precambrian rift magmatism of the Siberian Platform, in: Rift Magmatism: Petrology, Evolution, and Geodynamics [in Russian]. Nauka, Moscow, pp. 60–76.

Shpunt, B.R., Shapovalova, I.G., Shamshina, E.A., Lazebnik, K.A., Savvinov, V.T., Permyakov, E.D., Kelle, E.Ya., Yankovskii, E.V., 1979. The Proterozoic Strata of the Northeastern Margin of the Siberian Platform [in Russian]. Nauka, Novosibirsk.

Shpunt, B.R., Shapovalova, I.G., Shamshina, E.A., 1982. The Late Precambrian Strata of the Northern Siberian Platform [in Russian]. Nauka, Novosibirsk.

Smetannikova, L.I., Grinenko, V.S., Malanin, Yu.A., Prokopiev, A.V., Knyazev, V.G., Trushchelev, A.M., Yuganova, L.A., Zharikova, L.P., Kazakova, G.G., Shepelev, N.G., Yagnyshev, B.S., 2013. State Geological Map of the Russian Federation. Scale 1:1,000,000 (Third Edition). Anabar-Vilyui Series. Sheet R-51 (Dzhardzhan). Explanatory Note [in Russian]. Kartograficheskaya Fabrika VSEGEI, St. Petersburg.

Sun, S.-S., McDonough, W.F., 1989. Chemical and isotopic systematics of oceanic basalts: implications for mantle composition and processes, in: Saunders, A.D., Norry, M.J. (Eds.), Magmatism in the Ocean Basins. Geol. Soc. Lond. Spec. Publ. 42, 313–345.

Taylor, S.R., McLennan, S.M., 1985. The Continental Crust: Its Composition and Evolution. An Examination of the Geochemical Record Preserved in Sedimentary Rocks. Blackwell Scientific, Oxford.

Tkachenko, V.I., 1994. The Cambrian strata of the Kolyma-Omolon microcontinent. Izvestiya Vuzov. Geologiya i Razvedka, No. 1, 1–11.

Wang, K., Plank, T., Walker, J.D., Smith, E.I., 2002. A mantle melting profile across the Basin and Range, SW USA. J. Geophys. Res. 107 (B1), DOI: 10.1029/2001JB000209.

Williams, I.S., 1998. U–Th–Pb geochronology by ion microprobe: applications of microanalytical techniques to understanding mineralizing processes. Rev. Econ. Geol. 7, 1–35.

Winchester, J.A., Floyd, P.A., 1977. Geochemical discrimination of different magma series and their differentiation products using immobile elements. Chem. Geol. 20, 325–343.

Zindler, A., Hart, S., 1986. Chemical geodynamics. Ann. Rev. Earth Planet. Sci. 14, 493–571.